5.0 SITE RESPONSE

Bedrock ground motions propagating from the Teton fault will be modified by the soil column underlying much of Jackson Lake Dam. Recordings of strong ground shaking at the dam that would be needed to directly estimate this effect do not exist. As a practical matter, since nearby large earthquakes occur infrequently, only the weak-motion recordings from smaller, more frequently occurring earthquakes are available. We use this information, in conjunction with the material properties of the soil column (including drill-hole logs and seismic velocity profiles), to predict how these materials are likely to behave during M ~7 earthquakes on the Teton fault to develop realistic input motions for use in non-linear soil response models of strong ground shaking. The theoretical predictions are constrained by observations from weak-motion recordings made at the dam.

5.1 Weak-Motion Site Response

This section describes measurement of the weak-motion site response at Jackson Lake Dam. Ground motions from moderate-magnitude local earthquakes were recorded by three-component broadband velocity seismometers at six locations on the dam and one location on the right abutment.   Seismometers were deployed in an array along the axis of the dam, and in a linear array trending perpendicular to the dam. In order to estimate the weak-motion site response, recordings were compared to reference sites using the method of spectral ratios.

Ground motions on the north dike at stations 24+00 (JLD3, JLD4, and JLD5), 30+95 (JLD6), and 52+00 (JLD7) are amplified in the frequency range of 0.2 to 1.5 Hz, in comparison to the right abutment (JLDW). The duration of ground shaking in this frequency band is substantially prolonged. Ground motions at station 13+00 (JLD2) are not similarly amplified over this frequency range, nor are the durations appreciably prolonged. Shallow sedimentary basins can generate surface waves and converted body waves which result in this type of extended duration site response. Low-velocity fluviolacustrine sands, gravels and a northward thickening wedge of fines overlie higher-velocity glacial drift and gravels below the north dike (for stations greater than 14+00), which effectively produces a low-velocity sedimentary basin structure.

The amplification and prolonging of durations observed at station 24+00 (JLD3) were not observed at station 13+00 (JLD2), consistent with the higher shear-wave velocities measured in the soil column there. The transition in site response observed between stations 13+00 and 24+00 may occur close to station 14+00 based on the low shear-wave velocity observed at DH-804/805 (Sirles, 1986).

High-frequency (>1.0 Hz) ground motions recorded directly above the treated embankment foundation at station 24+00 (JLD4) are observed to be lower in amplitude than outside of the treated zone (JLD3), consistent with the higher shear-wave velocities obtained from the dynamic compaction and Soil Mix Wall (SMW) treatments (Wright, 1990). However, for frequencies below 1.0 Hz, substantial amplification and prolonging of duration are observed both inside and outside of the treated zone.

Poorly consolidated sands and gravels underlie much of the north dike of Jackson Lake Dam, and the site response to strong shaking is expected to be non-linear, in contrast to the observed weak motion response. However, both the weak and strong motion responses are influenced by the same shallow depositional basin structure underlying the dam.

While the observed weak motion site response (amplification and prolonging of duration) is consistent with that of a shallow closed basin (2-D and 3-D response), it is not easily explained by a vertically-propagating shear-wave in a horizontally stratified soil column (1-D response). The response of a one-dimensional soil column is difficult to reconcile with the observed response on the dam, which appears to be characterized by surface waves and converted body-waves.

Available computer codes for estimating non-linear site response are based on propagating an incident body wave through a 1-D soil column. These codes will tend to underestimate the observed duration of shaking at Jackson Lake Dam because they do not fully account for the 2-D and 3-D response of the local sedimentary basin (converted phases, surface waves, etc.). In order to better account for the two or three-dimensional character of the observed weak-motion site response, yet employ available one-dimensional codes for estimating non-linear site response, we have used a hybrid approach. This approach incorporates the longer durations observed in the

weak motion data to modify the input motions for use in one-dimensional nonlinear computer codes.

5.1.1 Instrumented Sites. Seven three-component, broad-band velocity seismometers were intermittently deployed at Jackson Lake Dam over a six-year period. Three to six seismometers were deployed at localities along the north dike, and one was deployed on the right abutment as a reference site. These sites are labeled JLDW, and JLD2 through JLD7 (see Figure 5‑1), and are described as follows:

JLDW: Located on Huckleberry Ridge Tuff on the right abutment, about 450 ft (140 m) from the south dike (approx. Station 03+00). This site is located in an old quarry that was used to provide rip rap for the dam. The Huckleberry Ridge Tuff appears to be about 70 to 100 ft (20-30 m) thick at this locality.

JLD2: Toe of the north dike 300 ft (100 m) to the left of the concrete section at about station 13+00, near where the roadway diverges from the top of the north dike. The seismometer is about 10 feet (3 m) downstream of the downstream Soil Mix Wall (SMW).   Figure 5-2 shows a cross-section of the dam near JLD2. Shear velocity profiles for the nearest drill hole pairs DH-800A/806 and DH-804/805 are shown in Figure 5-3. The profile for DH-800A/806, which has higher velocities, appears to be more representative for JLD2 because of the similarity of the observed site response to JLDW.

JLD3: Downstream from the toe of the north dike, at Station 24+00. This site is about 100 ft (30 m) downstream from the break in slope at the base of the embankment. It is located about 30 ft (10 m) away from the edge of the downstream SMW (Figure 5-2). No velocity profiles are available for JLD3-5, however the similarity of profiles at DH-804/805 and DH-807/808 (Figure 5-3) for the upper 100 feet (30 m) suggests that the velocity profile at JLD3-5 would be similar, at least for the upper 100 feet.
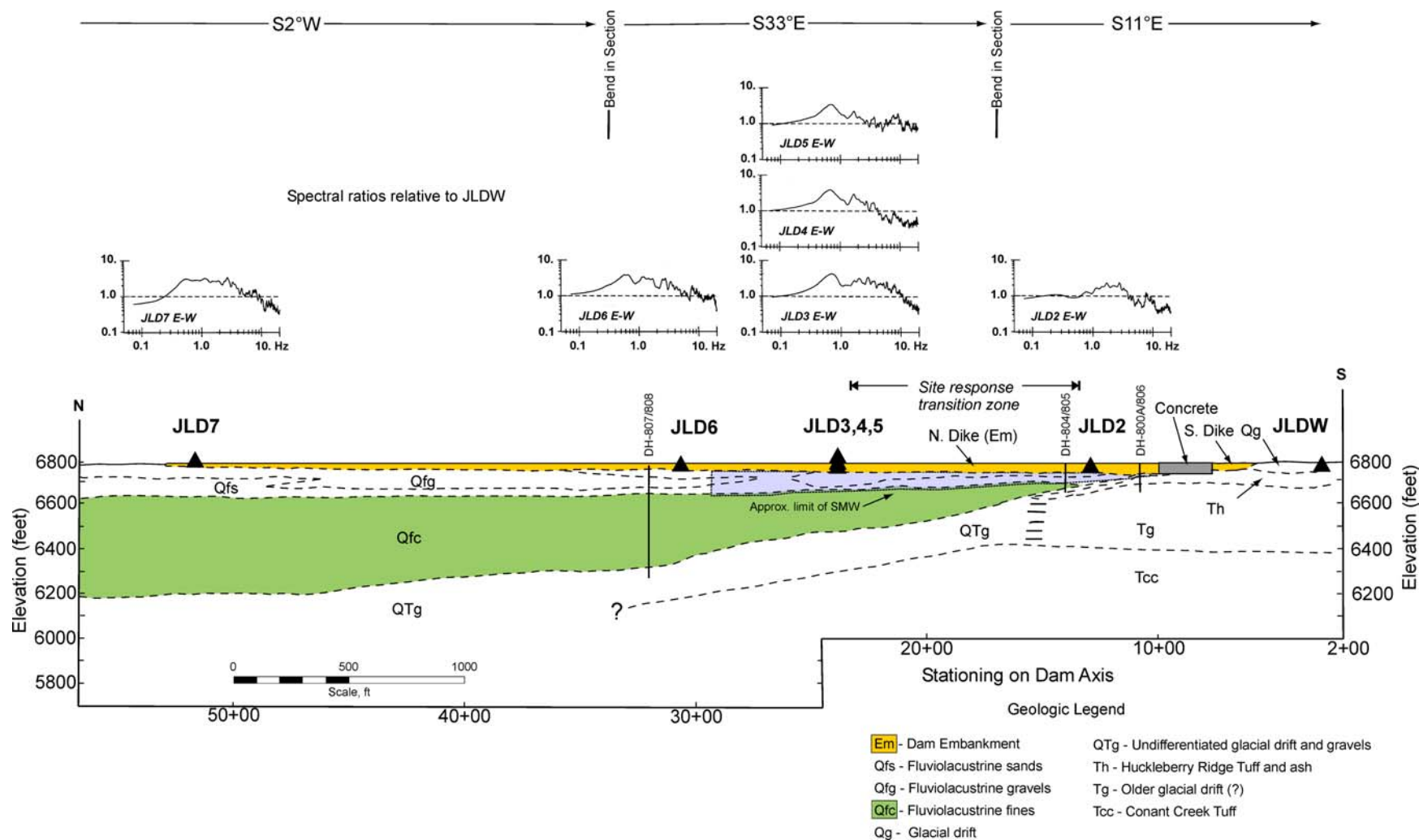
Figure 5-1: Jackson Lake Dam section showing locations of site response seismometers JLDW-JLD7. Average spectral ratios relative to JLDW measured from weak-motion data are also shown (east-west component). JLD3 through JLD7 exhibit amplification for frequencies between 0.2 and 1.0 Hz, whereas JLD2 does not. Transition between JLD2 and JLD3 response may occur as soon as DH-804/805 (stn. 14+00) since Qfs/Qfg shear-wave velocities measured there are much lower than measured at DH-800A/806, but are similar to shear velocities measured at DH-807/808. See Section 1.3.1 for additional discussion of site geology
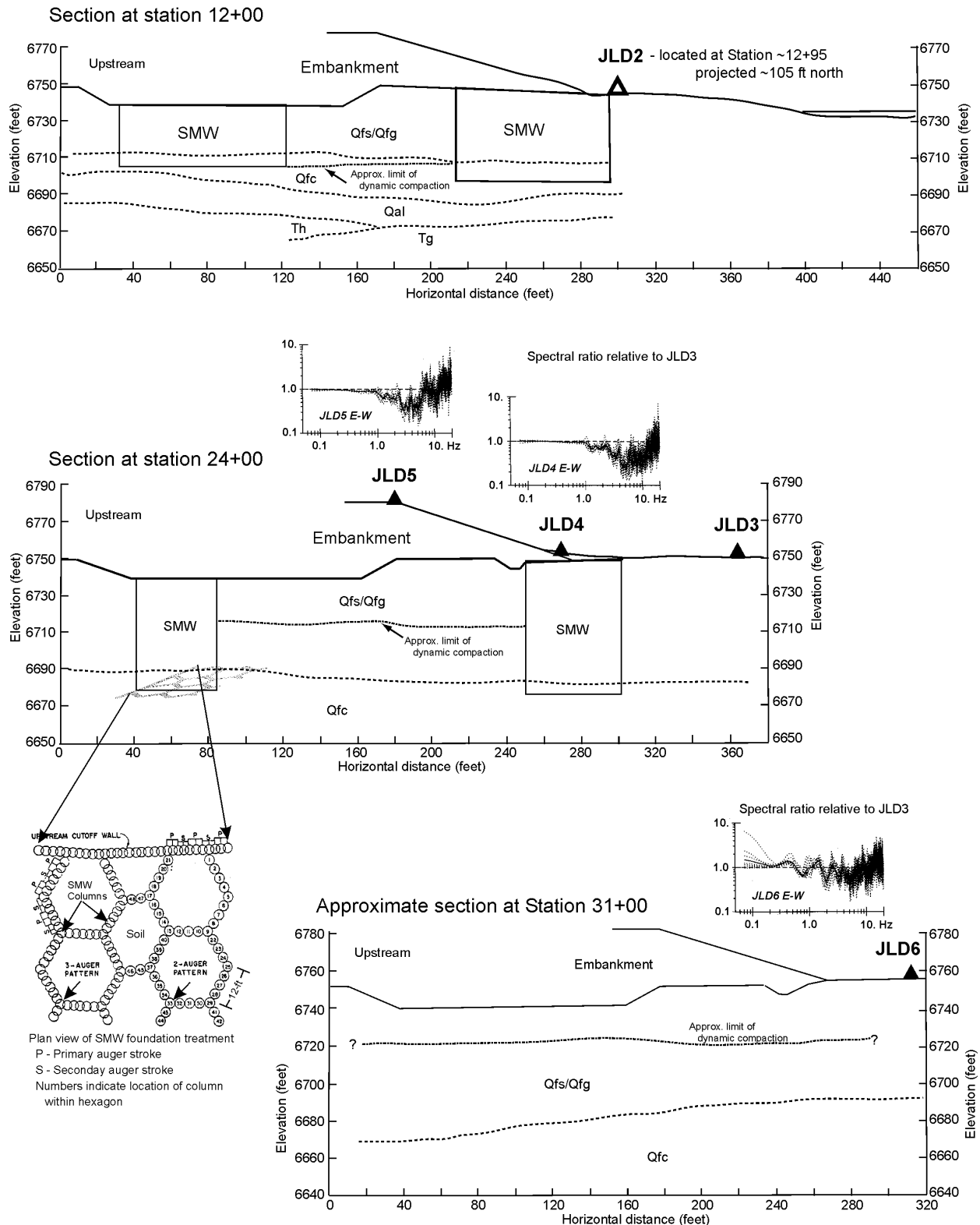
128

Figure 5-2: Profiles across Jackson Lake Dam at stations 12+00, 24+00, and 31+00 (Stelma, 1996) showing location of site response seismometers JLD2 through JLD6. Single-event spectral ratios relative to JLD3 are shown, indicating a de-amplification effect of foundation treatment for frequencies above 1.0 Hz.
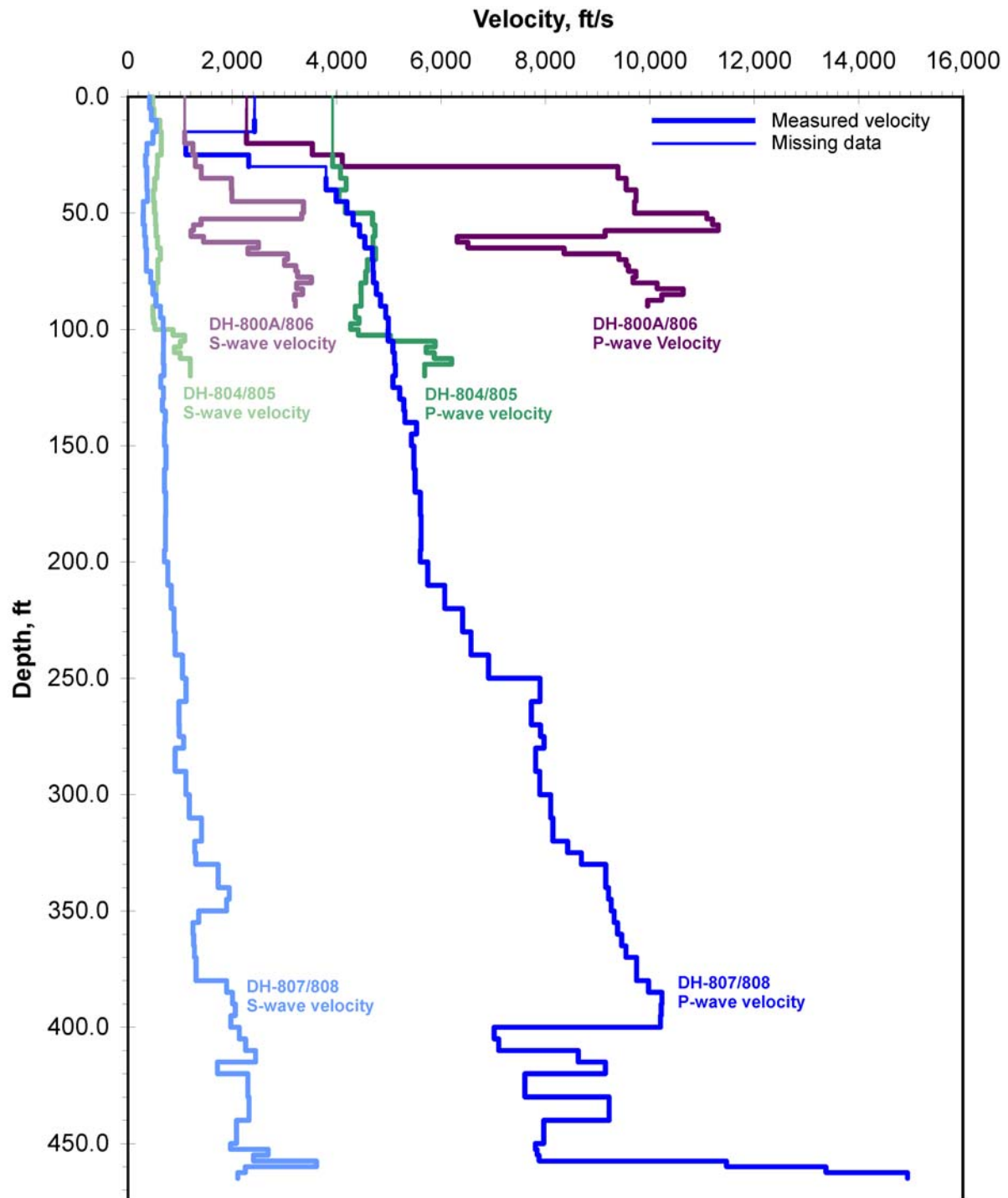
Figure 5-3: Compressional and shear wave velocity profiles for the soil column underlying the north dike of Jackson Lake Dam, as determined by crosshole velocity measurements (Sirles, 1986). See Figure 5-1 for location of drill holes. Zero-level for profiles is approximately the level of the upstream toe of the north dike. For DH-800A/806, which was drilled from the crest of the dike, the profile reported by Sirles (1986) was shifted by 25 feet. The other profiles were drilled from the upstream toe

JLD4: Toe of the north dike at Station 24+00. This site is located at the downstream edge of the embankment. The top of the downstream SMW lies a few feet below the site (Figure 5-2).

JLD5: Crest of the north dike at Station 24+00. This site is located at the downstream edge of the roadway on the crest of the dike (Figure 5-2).

JLD6: Toe of the north dike at Station 30+95. This site is located 57 ft (17 m) downstream from the embankment, about 20 ft (6 m) outside of the limit of the Stage I dynamic compaction zone (Figure 5-2). DH-807/808 is near JLD6. The velocity profile is shown in Figure 5-3.

JLD7: Toe of the north dike at Station 52+00. This site is located 5 ft (2 m) downstream from the embankment. The Stage I dynamic compaction zone extends approximately to station 52+00, and JLD7 is near the boundary, perhaps up to 10 ft (3 m) outside of the compaction zone. Groundwater encountered just below the ground surface prevented placement of the seismometer vault much beyond or downstream from this point. No shear-wave velocity profile is available at JLD7.

Initially, each seismometer (Guralp model CMG-40T) was installed below grade on a 2-ft (0.5 m) diameter plaster pad covered by a lightweight plastic vault. The pad for JLDW was cemented onto an outcrop of Huckleberry Ridge Tuff. The top of each vault was buried about 6 in (15 cm) below grade, and covered with soil for thermal stability. Conduit was extended from the seismometer vaults to nearby fiberglass instrumentation enclosures that served to house digital event recorders and other equipment.

Flooding problems during the spring snowmelt and runoff eventually required abandonment of many of the subsurface vaults. While the vaults, seismometers and cables were watertight, they were not designed for long term immersion and eventually leaked or corroded. Flowing water was observed just a few inches below the ground surface at stations JLD3, JLD6, and JLD7. These vaults flooded on several occasions, requiring uncovering, draining, cleaning, and resealing.

Because of flooding problems, the seismometers at stations JLD2, JLD3, JLD5 and JLD6 were eventually relocated above ground, to the inside of nearby fiberglass instrumentation enclosures. The data logging instrumentation was also upgraded. The above ground enclosures did not provide the thermal stability of the subsurface vaults, but the seismometers remained dry. These fiberglass enclosures also housed the strong-motion instrumentation for the dam. Each fiberglass enclosure was bolted to a 5-ft x 5-ft x 6-in concrete pad that had been poured on grade. The relocated seismometers from JLD2, JLD3, and JLD5 were placed on the concrete pads, inside of the enclosures. The subsurface vault for JLDW remained dry, and the seismometer there was not relocated. The seismometers for JLD4 and JLD7 were eventually removed because there were no adjacent strong-motion enclosures to relocate the seismometers into.

5.1.2 Initial Data Recording System. Instrumentation for the initial deployment consisted of Guralp CMG-40T seismometers attached to 16-bit digital event recorders (RefTek Model A72-06), each with an internal 1-Gbyte disk drive. Identical instrumentation was installed at seven sites (JLDW and JLD2-7). The RefTek recorders have unity and x32 gain inputs for each component, providing a nominal 120 dB dynamic range. Reference timing was obtained from GPS receivers attached to each digital event recorder. Seismometer calibration was obtained from the manufacturer. Differences in the calibrated response for all the sensors used in this study were minor, apart from an overall gain factor.

The Guralp CMG-40T sensors used in this study had a corner frequency of 30 seconds (velocity output), which allowed for adequately recording motions in the frequency range of engineering interest (0.2 to 2 Hz). However, background noise for unfiltered seismograms was typically dominated by long period (> 6 seconds) microseisms. In contrast, the predominant frequency content of small local earthquakes was typically greater than 1 Hz.

The broad-band frequency response of the seismometers thus had a significant impact on the triggering algorithm used by the RefTek digital event recorders because they lacked any provision for adequate high-pass filtering of the data stream used for event detection. Only local events producing amplitudes much greater than the background long-period microseismic noise could be consistently recorded. High-frequency local earthquake waveforms riding on top of the low-

frequency microseisms were not consistently detected, resulting in reduced efficiency of data collection.

Each of the RefTek digital event recorders at the dam operated independently of one other, and from the regional seismic network. This had a further limitation on the efficiency of event detection and recording because it prevented real-time correlation of triggers from the individual stations in declaring an event trigger. Correlation of station triggers provides a powerful tool for earthquake event detection in seismic networks. But correlation was not possible at the time of recording, and hence numerous noise triggers were recorded because noise and seismic triggers were not readily distinguished by the event recorders. The resulting low ratio of seismic triggers to noise triggers required considerable post-processing efforts to retrieve usable data.

Because seismic noise levels tended to vary substantially between the seven sites due to differences in proximity to highway traffic, wind and water noise, site conditions, etc., smaller events would rarely trigger all event recorders simultaneously. Instead, only a subset of the digital event recorders might trigger for any particular event. Operating seven separate GPS receivers for each event recorder also proved to be less reliable because of intermittent temperature related failures of some receivers. Trigger levels for the individual recorders were adjusted to capture the greatest number of local events

Approximately 60,000 individual station triggers were obtained from the seven sites at the dam, the vast majority being noise triggers unrelated to earthquakes. This volume of data required an automated method for post processing. Post-processing of the individual station triggers initially consisted of correlating similar trigger times, and combining the separate station triggers into an event trigger if at least three of the seven stations had triggered. However, it soon became apparent that most of these event triggers were also noise, albeit correlated between stations (e.g., from highway traffic). After thoroughly examining a subset of the digital event recorder triggers, it appeared that most seismic triggers recorded at the dam resulted from local earthquakes that had also been well-recorded by the regional seismic network. The seismic network was thus used to establish specific time windows for seismic events for the remainder of data recorded by the event recorders. Consequently, only triggers from stations at the dam which also correlated with the origin times of local earthquakes as determined by the regional seismic network were considered.

These potential triggers were reviewed by hand, and if confirmed to be seismic in origin, were merged into the waveform data from the seismic network for further processing. This process resulted in a data set consisting of about 270 local earthquakes with epicentral distance ranging between 5 and 110 km, and magnitude ranging between 1.2 and 3.9.

5.1.3 Upgraded Data Recording System. Technology advances allowed for site response data to be collected much more reliably and with far less effort needed for post-processing. The 16-bit RefTek digital event recorders and stand-alone Guralp sensors were replaced by 24-bit digital-output broadband seismometers (Guralp DM-24). Real-time continuous digital data telemetry via frame relay was extended to the dam. The continuous data streams from four seismometers at the dam (JLDW, JLD2, JLD3, and JLD5) were automatically merged into the data streams for the regional seismic network data acquisition system. Common time stamping was provided by a single GPS receiver located at the dam.

The upgraded instrumentation allowed for more reliable data collection because any earthquake that triggered the regional seismic network would automatically trigger simultaneous data recording from all the site-response sensors at the dam. Over the 8-month period that the upgraded instrumentation collected data, about 150 local earthquakes were recorded, with magnitude ranging between 1.0 and 3.6. This rate of data collection using the upgraded system was thus about three times greater than obtained using the RefTek system. All data were recorded on a common time base, and the seismic traces from the network stations were automatically merged with the site response stations, which greatly reduced the time needed for routine analysis tasks.

A final benefit of the improved system was to allow for long codas (> 90 seconds) to be recorded. Post-trigger waveforms on the RefTek system were limited to 60 seconds to prevent overrunning of the storage system from noise triggers. In contrast, the upgraded system allowed for improved estimates of duration and spectral amplification by recording longer codas.

5.2 Observations

From 1996 through 1999, using the initial RefTek recording system, approximately 270 local earthquakes were recorded by one or more site-response instruments. Of these earthquakes, just 6

were simultaneously recorded by all seven instruments (Table 5-1). The upgraded recording system was installed and became operational in October, 2000, and included four of the previous seven sites (JLDW, JLD2, JLD3, and JLD5). Data was acquired more rapidly and reliably, with 150 events simultaneously recorded on all four instruments over the next eight months. In June, 2001, a minor equipment failure halted the flow of data from JLD2, JLD3, and JLD5, and it was not possible to carry out the necessary repairs. However, data continued to be collected from JLDW along with the regional seismic network until December, 2002, when all recording of the seismic network ceased.

Table 5-1: RefTek Data Collection Summary

RefTeks triggered simultaneously.	Number of local earthquakes.
7	6
6+	14
5+	65
4+	136

5.2.1 Waveform Data Results. From the velocity waveforms recorded by the site response instruments, several characteristics of the weak-motion site response are apparent. Long period ground motions (1.0 to 5.0 seconds) are amplified and prolonged on the north dike of the dam, compared to bedrock motions on the right abutment.

Figure 5-4A shows a typical waveform recorded by the upgraded instrumentation, and is from an **M** 3.2 earthquake located near Driggs, Idaho (epicenter approximately 45 km west of the dam). The uncorrected, unfiltered east-west velocity waveforms (95-second time window) for JLDW, JLD2, JLD3 and JLD5 are shown in Figure 5-4A. Figure 5-4B shows the same data, but bandpass-filtered between 0.2 and 1.0 Hz. In both the unfiltered and filtered data, JLDW and JLD2 have similar waveforms, with some enrichment in high-frequency (> 1.0 Hz) ground motions at JLD2 after the direct S-wave. In contrast, ground motions at JLD3 and JLD5 have considerably more long-period (> 1 s) energy, with several phases arriving 40 seconds after the direct S-wave that considerably extend the duration of shaking. While the amplitude of long-period shaking for this event decreases by a factor of two within 10 seconds for the direct S-wave

at JLDW and JLD2, it takes nearly 50 seconds for a similar decrease to be seen at JLD3 and JLD5.

Figure 5-4C shows the instrument-corrected Fourier amplitude spectrum of east-west displacement for JLDW, and the spectral ratios (referenced to JLDW) for JLD2, JLD3, and JLD5. The methodology is described in Section 5.2.2. Spectral ratios for JLD3 and JLD5 for this event reach a value of about 5 at a frequency of 0.7 Hz; below 0.2 Hz, the ratios are near unity. The spectral ratio for JLD2 does not exhibit a similar long-period peak; the ratio is near unity for frequencies below about 1.0 Hz, and there are numerous peaks and valleys above 1.0 Hz.

Figure 5-5 shows another example, this time for an **M** 3.1 earthquake located 34 km southeast of the Jackson Lake Dam in the Gros Ventre Range. This earthquake was recorded by the initial
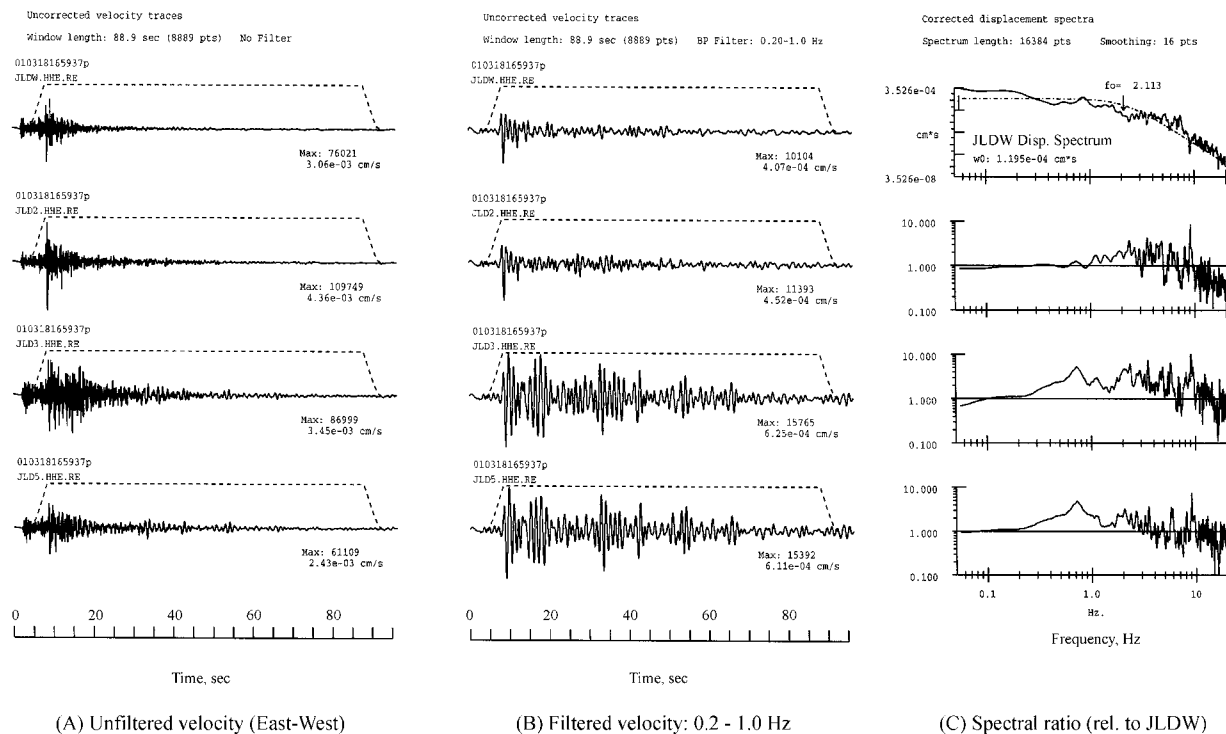

(A) Unfiltered velocity (East-West)   (B) Filtered velocity: 0.2 - 1.0 Hz   (C) Spectral ratio (rel. to JLDW)

Figure 5-4: M 3.2 earthquake located near Driggs Idaho. Epicentral distance is 45 km. (A) Unfiltered, uncorrected velocity; (B) Bandpass filtered 0.2 – 1.0 Hz, uncorrected velocity; (C) Corrected Fourier amplitude spectrum of displacement (JLDW), and spectral ratios referenced to JLDW. Prolonged duration of shaking for frequencies less than 1.0 Hz is clear in (B). JLD2 has a spectral ratio near unity for f < 1Hz. JLD3 and JLD5 show pronounced amplification for f < 1Hz.
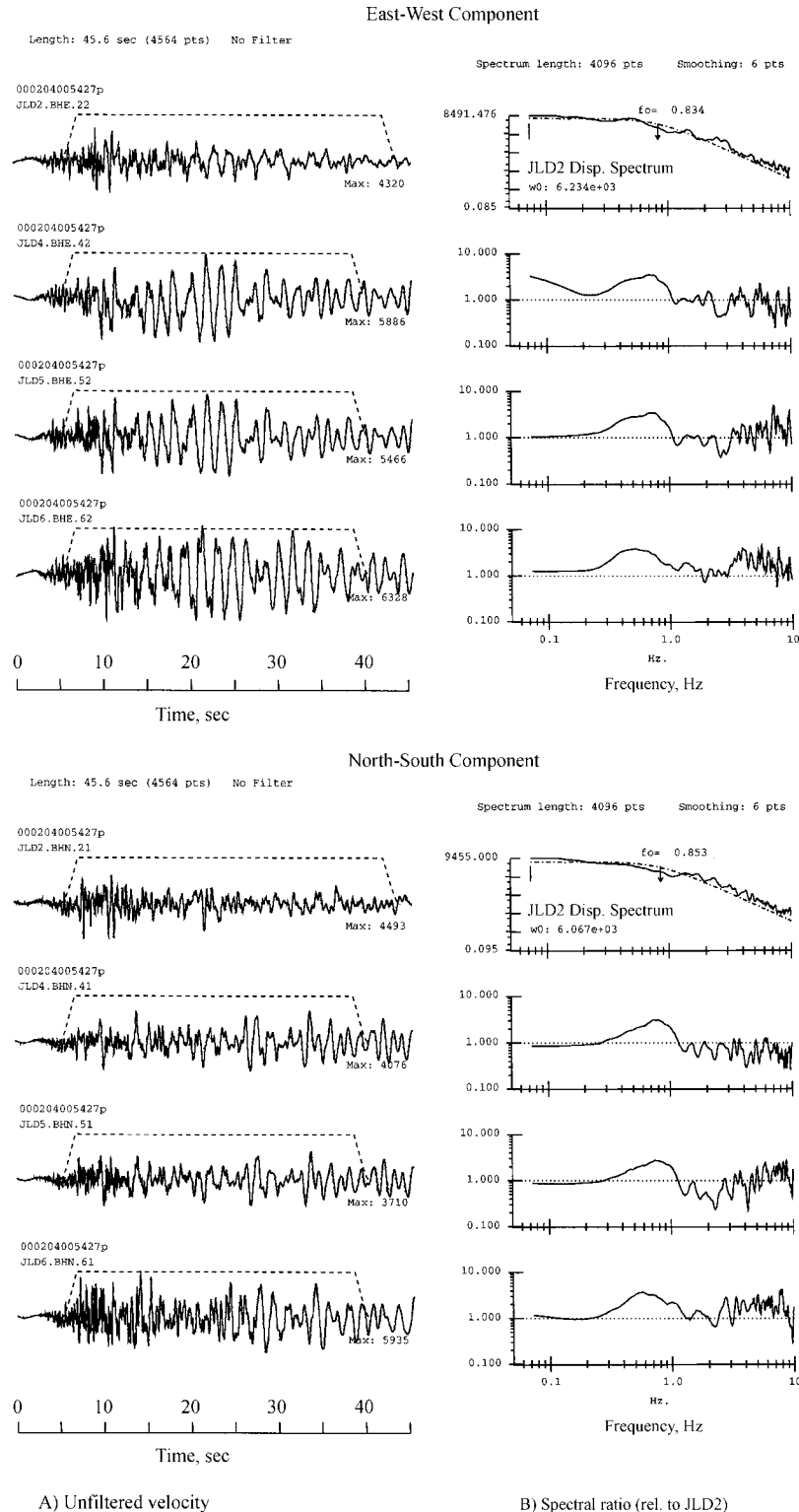
Figure 5-5: M 3.1 earthquake located 34 km southeast of the Jackson Lake Dam in the Gros Ventre Range. (A) Unfiltered velocity waveforms; (B) Corrected Fourier amplitude spectrum of displacement (JLD2), and spectral ratios referenced to JLD2. Amplification of <1.0 Hz frequencies relative to JLD2 is readily seen in the unfiltered velocity traces.

instrumentation (which relied on the RefTek digital event recorders), and has a shorter data window (40 seconds) than the first example. While the low-pass filtered direct S-wave pulse has a similar shape on JLDW, JLD2, JLD4 and JLD5, the waveforms are markedly dissimilar after the first few seconds. The amplitude actually increases about 5 seconds after the direct S arrival at JLD4 and JLD5, and large amplitude phases continue to appear up through the end of the data window some 35 seconds later. The amplitudes of the band-pass filtered seismogram at JLD4 and JLD5 are about a factor of 2 to 3 times greater than observed at JLDW or JLD2.

Prolonged duration of shaking is commonly attributed to basin response (e.g., Osborne and Taber, 2000), since a soil column by itself does not lead to appreciable increases in duration on soil sites compared to rock sites (Bommer and Martinez-Pereira, 1999).

5.2.2   Spectral Ratio Method. We used the method of spectral ratios (Borcherdt, 1970; Field et al., 1992; Field and Jacob, 1995) to evaluate weak motion site response. The Fourier amplitude spectra of the S-wave and coda at seismometer sites on the dam were compared to nearby reference sites. This method assumes that the earthquake source and propagation effects are nearly the same for all sites. This assumption appears to be satisfied since the overall dimension of the array is less than 2 km, while typical epicentral distances for the events analyzed are 20 km or more, and the source dimension of the earthquakes was small. We calculated spectral ratios separately for the vertical, north-south and east-west components of motion at each of the 6 sites on the dam (JLD2-7) referenced to the right abutment site JLDW. We also computed spectral ratios using other selected subsets of stations and reference stations (e.g., JLD3-7 referenced to JLD2, and JLD4-7 referenced to JLD3).

Fourier amplitude spectra for the direct-S and coda were calculated for each event using the following procedure. First, each data trace was de-meaned and box-car windowed, starting about 1 second before the picked direct S arrival for that station. A time-domain Hanning (cosine) taper was then applied to the initial and final 10% of the window (Bartlett, Parzan, and Blackmann-Harris tapers were also tried but made little difference). The start time of the pre-S part of the window was selected so that the taper reached a value of one by the time of the S arrival. The mean was removed (again) from the tapered trace, zero-padded to the next power of two, and Fourier transformed using an FFT. The amplitude and phase were further smoothed in the

frequency domain by using a 3 to 25-point triangular window, depending on the length of the FFT. The smoothed spectra were then corrected for instrument response, using calibration data provided by the manufacturer, converted to displacement, and corrected for relative gain between instruments. The phase spectra were also unwrapped.

The response of the Guralp sensors used throughout this study was nominally flat to velocity between 30 seconds and 50 Hz, and the data were sampled at 100 Hz, however, we have focused on a 20-second to 20 Hz bandwidth for the spectral ratios to maintain good signal to noise ratios.

Ratios of the smoothed spectra for specific events were computed using the following procedure. First, if the window length of the reference trace differed from that of the comparison trace, a further correction equal to the square-root of the ratio of the input data window lengths was applied to the Fourier amplitude spectrum. Next, the ratios of the amplitude spectra were computed, and logarithms taken. The difference between the unwrapped phases of the comparison and reference station was also computed.

Mean spectral ratios were computed by taking the mean of the logarithms of the spectral ratios for the selected events, with the vertical and two horizontal components treated separately.

We considered but did not implement the cross-spectral ratio method of Safak (1991; 1997) for computing spectral ratios. There have been questions raised about the accuracy of the cross-spectral approach because of signal-induced noise such as scattering (Field et al., 1992). While those concerns were addressed by Safak (1997), the examples presented by Safak (1997) comparing both methods indicate that differences between the two methods are likely less than other sources of uncertainty. Thus, we have chosen to use the direct method of computing spectral ratios. We also did not use the generalized inverse method of computing site response spectra (Andrews, 1986) since it also appeared to offer minimal advantage over the direct spectral ratio method (Field and Jacob, 1995).

5.2.3 Average Spectral Ratios. Station spectral ratios were obtained by averaging, for each of the three components of motion, the single-event spectral ratios. Averages for the vertical and two horizontal components of motion were determined separately for each station.

Figure 5-6 shows the spectral ratios for the east-west and north-south components of motion for the 29 events that were well recorded at JLDW through JLD7. The spectral ratios are referenced to JLDW, and both individual and average station spectra are shown. It is apparent from Figure 5-6 that stations JLD2-JLD7 are amplified by a factor of 2 to 5 at various frequency bands ranging from 0.2 to 4.0 Hz, referenced to JLDW. For both the north-south and east-west components of motion, there is a similar broad pattern of amplification. The site amplification observed at JLD2 differs from JLD3-7 in at least one important respect. At JLD2, the amplification is for frequencies above 1.0 Hz, whereas at JLD3 through JLD7, the site amplification is for frequencies above 0.2 Hz. Thus stations JLD3-7 show much more broadband amplification than does JLD2, relative to JLDW.

The spectral ratios for JLD3-JLD7 at low frequencies (0.2 to 0.1 Hz) consistently show site amplification of about a factor of 3 to 5, referenced to JLDW. In comparison, the spectral ratio for JLD2 in this frequency range is approximately unity. Thus JLD2 has relatively little long-period site amplification, with respect to JLDW, which is in contrast to the amplification observed at JLD3-7.

JLD2 is located at station 13+00, about 15 feet (5 m) downstream from the toe of the north embankment. The underlying soil column at JLD2 consists of a thin layer of fluviolacustrine fines overlying gravels and Pliocene rocks. JLD2 is also located at the edge of the SMW zone underlying the south half of the north dike. In contrast, at JLD3-7, the underlying soil column consists of about a 100-ft (30 m) thick layer of poorly consolidated sands and gravels overlying a 200 to 400 ft (60 to 120 m) thick layer of fluviolacustrine fines. While JLD4 and 5 are also within the SMW zone (see Figure 5-2), the pattern of long-period amplification persists, apparently the result of a thicker column of lake deposits and a position further within the sedimentary basin.

Figure 5-7 shows the average spectral ratios for the east-west and north-south components of motion at JLD2, JLD3 and JLD5, relative to JLDW, for 24 earthquakes recorded by the upgraded instrumentation. The upgraded system allowed for consistently recording longer time windows at 24-bit resolution, and thus provided data recorded at the best fidelity, although at a smaller number of locations. The same pattern of long-period amplification at JLD3 and JLD5 (with little
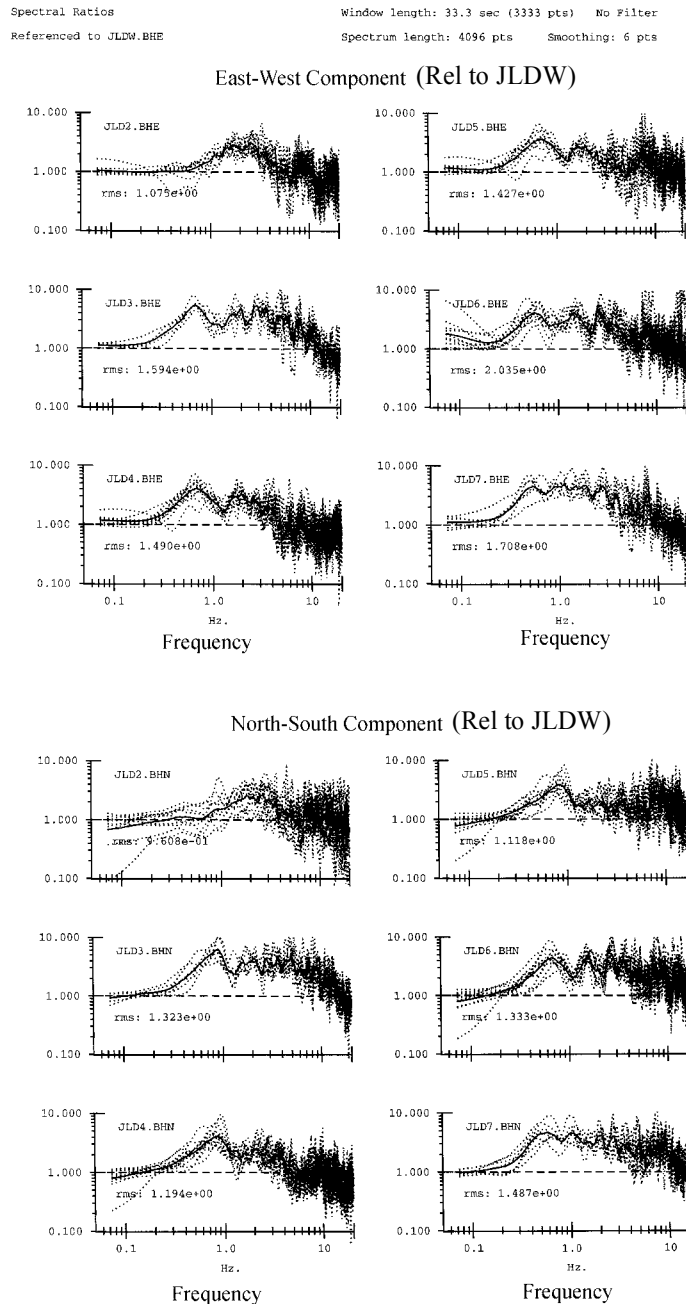
Figure 5-6: Spectral ratios relative to JLDW for 29 earthquakes recorded by the RefTek instrumentation initially deployed at seven sites (JLDW through JLD7). Solid line indicates average of individual spectral ratios; dashed lines are spectra from individual events. At low frequencies (f < 1 Hz), the observed spectral ratios are consistent between earthquakes, which occur at several different azimuths. The east-west and north-south spectral ratios are also similar for each sensor location. JLD3 through JLD7 exhibit a consistent pattern of low-frequency (0.3 to 1.0 Hz) amplification, with a spectral peak at about 0.8 Hz.

```
Spectral Ratios                         Window length: 33.3 sec (3333 pts)   No Filter
Referenced to JLDW.HHE                  Spectrum length: 4096 pts      Smoothing: 6 pts
```

A) East-West Component Spectral Ratios (rel. to JLDW)

B) North-South Component Spectral Ratios (rel. to JLDW)
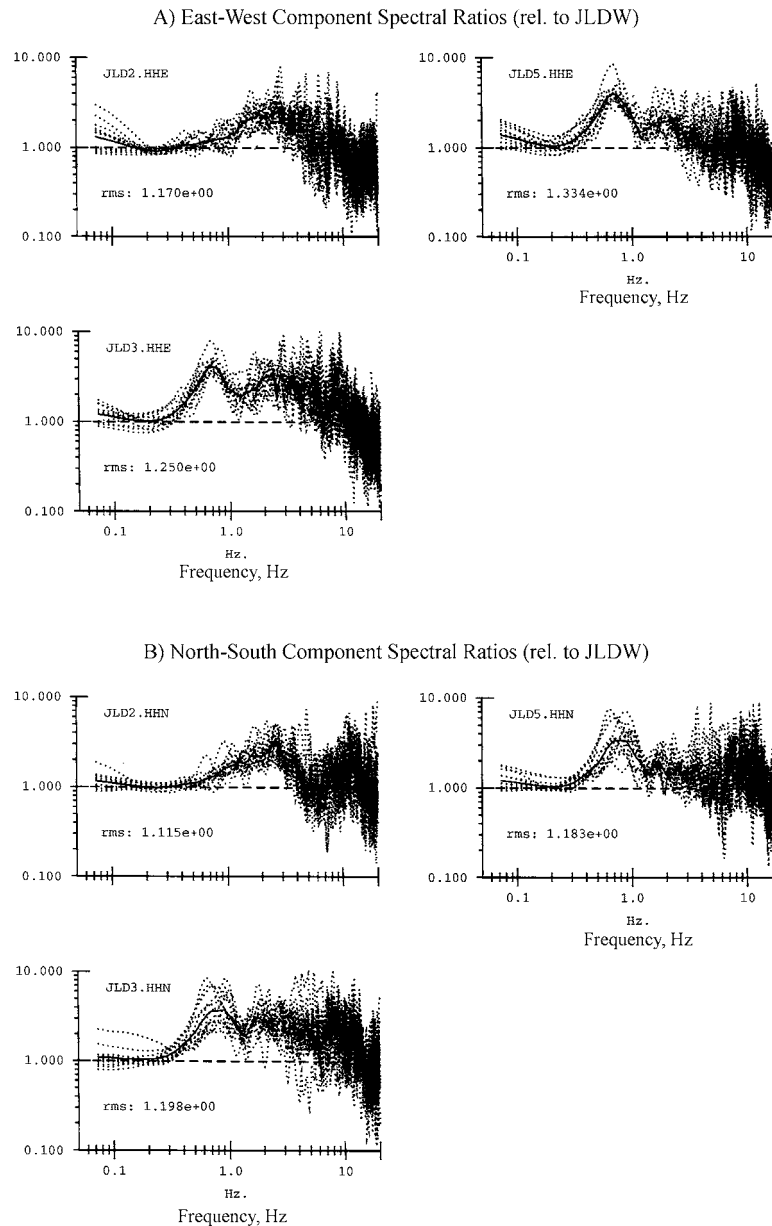
Figure 5-7: Spectral ratios relative to JLDW for 24 earthquakes recorded by the upgraded instrumentation deployed at sites JLDW, JLD2, JLD3, and JLD5. The upgraded instrumentation allowed data to be recorded with a wider dynamic range and spectral resolution than could be achieved with the RefTek instrumentation. Solid line indicates average of individual spectral ratios; dashed lines are spectra from individual events. At low frequencies (f < 1 Hz), spectral ratios are consistent between earthquakes, which occur over a range of azimuths and epicentral distances. As with the RefTek data, JLD3 and JLD5 exhibit low frequency amplification with respect to JLDW, whereas JLD2 does not.

or no long-period amplification at JLD2), that was seen in the earlier data is also readily apparent in the data collected by the upgraded instrumentation.

Average spectral ratios may also be used to compare the response of the five stations on the north dike (JLD3-7) that overly a 300-500 ft (90-150 m) thick column of fluviolacustrine deposits (Figure 5-1). Figure 5-8A shows spectral ratios at JLD4 through JLD7, referenced to JLD3, for the east-west component of motion. Figure 5-8B shows corresponding spectra for the north-south component of motion.

JLD3, JLD4 and JLD5 form a 177-ft (54 m) linear profile perpendicular to the north dike embankment at station 24+00 (see Figure 5-2). JLD3 is located 95 feet from the downstream edge of the north dike embankment, outside of the zone of dynamic compaction, and in other circumstances would be chosen as our "reference" soil site. JLD4 is 93 feet from JLD3, at the edge of the embankment, and overlies the downstream soil mix wall. JLD5 is 84 feet from JLD4 (177 feet from JLD3), and is at the crest of the embankment. The spectral ratios for JLD4 referenced to JLD3 show de-amplification for frequencies above 1 Hz; below 1 Hz, the spectral ratio is near unity. A similar pattern is seen for JLD5 referenced to JLD3, although the de-amplification above 1 Hz is less pronounced. The strongest de-amplification relative to JLD3 is seen at JLD4, which is consistent with the higher seismic velocities of the treated foundation (soil mix wall and dynamic compaction). A more limited de-amplification at JLD5 is consistent with the higher seismic velocities in the embankment and in the underlying dynamically compacted foundation, relative to JLD3, and the amplification typically observed at the crest of dams relative to the toe due to simple geometric focusing. However, at longer periods (>1 second), the response is similar at all three sites (JLD3, 4 and 5).

JLD6 is 20 feet (6 m) outside of the zone of dynamic compaction, and 57 feet (17 m) from the downstream edge of the embankment at station 30+95. The soil mix walls do not extend this far north, stopping at about station 29+00. JLD7 is 5 feet from the downstream edge of the embankment at station 52+00, and is located about 10 feet outside of the zone of dynamic compaction. Relative to JLD3, there is some long-period amplification at JLD6, and alternating amplification and de-amplification at frequencies above 1 Hz. JLD7 shows even greater long-

```
Spectral Ratios                    Window length: 33.3 sec (3333 pts)    No Filter
Referenced to JLD3.BHE             Spectrum length: 4096 pts      Smoothing: 6 pts
```
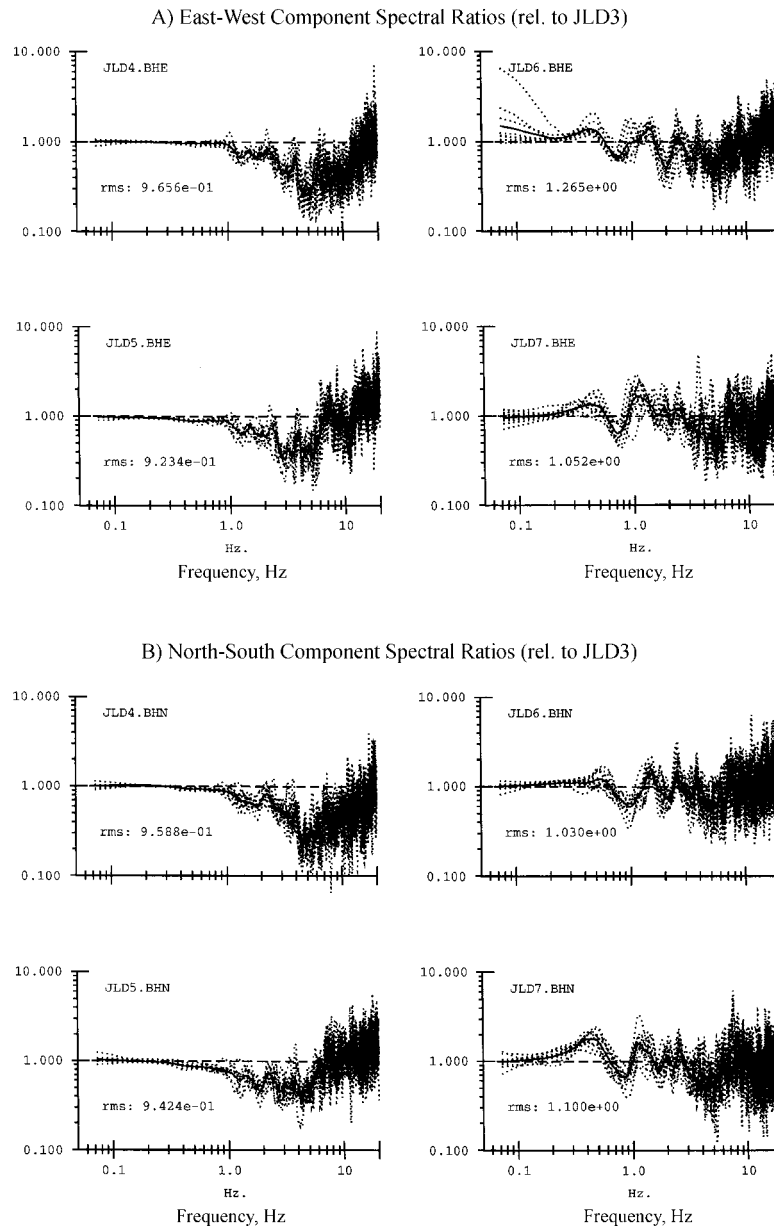

Figure 5-8: Spectral ratios relative to JLD3 for 29 earthquakes recorded by the initial deployment of RefTek instruments. Solid line indicates the average of individual spectral ratios. JLD4 and JLD5 exhibit a de-amplification effect relative to JLD3 for frequencies between about 1 and 10 Hz, which is consistent with the higher velocities achieved through foundation treatment (dynamic compaction and the Soil Mix Wall). Below 1 Hz, little meaningful difference is seen; each of stations JLD3, JLD4 JLD5 are amplified relative to JLDW.

period amplification than JLD6, relative to JLD3. This pattern is consistent with a deepening soil column at JLD6 and JLD7 relative to JLD3 (Figure 5-1).

Average spectral ratios relative to JLDW for all data recorded by the RefTek instrumentation are shown in Figure 5-9 and Figure 5-10. Stations JLD3 through JLD7 consistently show a spectral ratio amplification in the frequency range of 0.2 to 1.0 Hz, referenced to JLDW. In contrast, JLD2 shows no such long-period amplification.

There is a considerable difference in site amplification observed between JLD2 and JLD3-5, which are located about 1100 ft (340 m) apart, along the axis of the north dike. This difference has the potential to lead to significant axial strains between these two points. The magnitude of the strain will depend on the sharpness of the transition. From JLD3-5 to JLD7, which are 2800 ft (850 m) apart, there is relatively little difference in site response; long-period amplification is observed even though the soil column is deepening. JLD6, midway between JLD3-5 and JLD7, shows the same pattern. Thus there appears to be a point between JLD2 and JLD3-5 at which a sharp rather than gradual transition to long-period amplification may take place. It is not clear from the site-response data where the precise position of this transition is located, however shear wave profiles (Figure 5-3) suggest the transition may be closer to station 14+00.

5.3 Weak-Motion Impulse Response Functions

The previous sections provide a qualitative description of the observed weak-motion site response at Jackson Lake Dam. Key observations are the presence of substantial long-period amplification and prolonged duration of shaking beyond some transition point located between JLD2 and JLD3-5; minimal long-period amplification at JLD2 referenced to JLDW; and, high-frequency de-amplification at JLD4 and JLD5 referenced to JLD3.

To apply these findings to simulations of strong ground shaking from the Teton Fault, we have generated weak-motion site impulse response functions at stations 13+00 (JLD2) and 24+00 (JLD3) that are based on the observed average amplitude spectral ratio and the relative phase for average or specific earthquakes. For the amplitude part of the impulse response, we use the average spectral ratios described in the previous section (Figure 5-10). For the phase response, we selected several representative events and extracted the single-event relative phase response (the

Amplitude Spectral Ratios   Window length: 33.3 sec (3333 pts)   BP Filter: 0.15-20.0 Hz

Referenced to JLDW.BHE (win frac: 0.500)   Spectrum length: 4096 pts   Smoothing: 6 pts

A) East-West Component Average Spectral Ratios (rel. to JLDW)
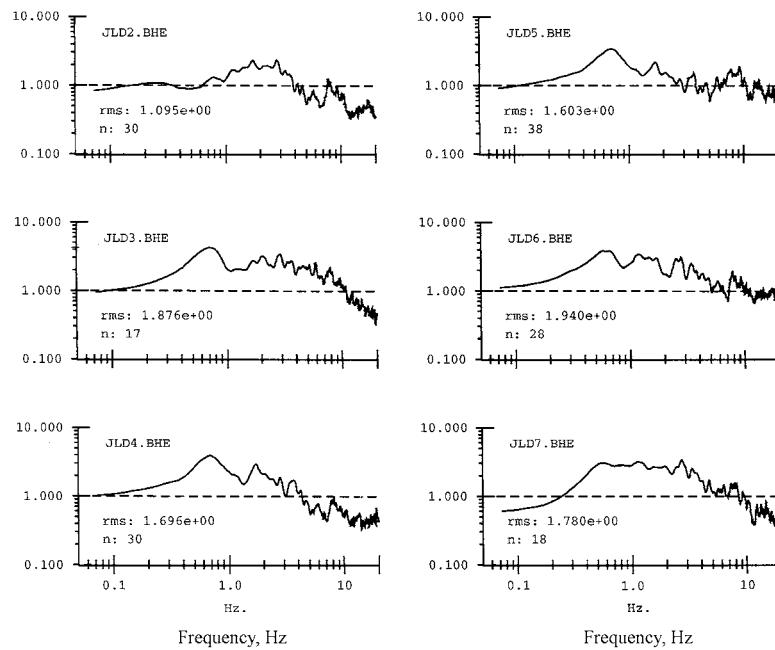
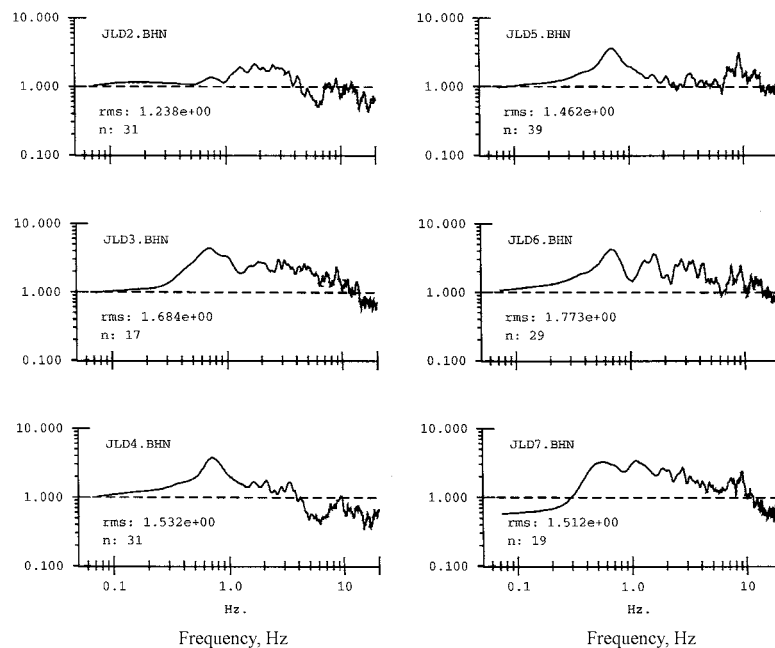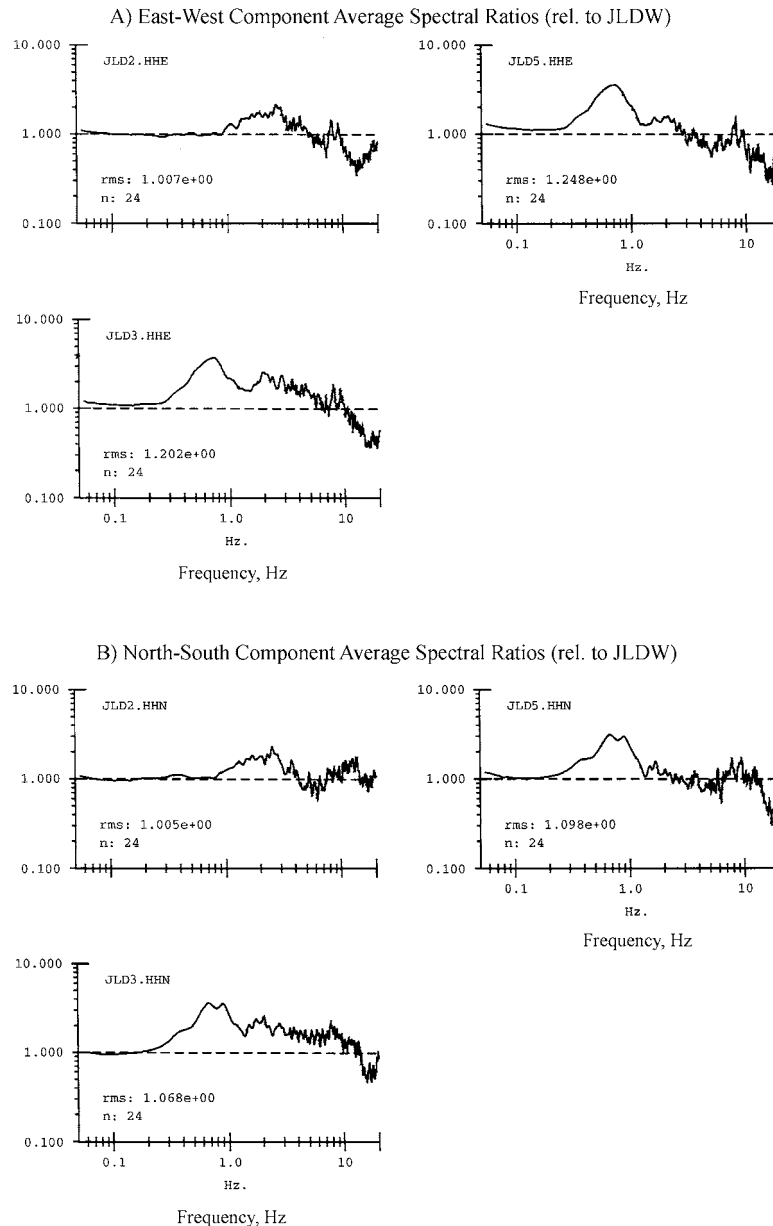B) North-South Component Average Spectral Ratios (rel. to JLDW)

Figure 5-9: Average spectral ratios relative to JLDW for 29 earthquakes recorded by the initial deployment of RefTek instruments.

Amplitude Spectral Ratios   Window length: 88.9 sec (8889 pts) BP Filter: 0.05-20.0 Hz
Referenced to JLDW.HHE (win frac: 0.500) Spectrum length: 16384 pts Smoothing: 16 pts

A) East-West Component Average Spectral Ratios (rel. to JLDW)

B) North-South Component Average Spectral Ratios (rel. to JLDW)

Figure 5-10: Average spectral ratios relative to JLDW for 29 earthquakes recorded by the upgraded instrumentation deployed at stations JLDW, JLD2, JLD3 and JLD5. JLD3 (station 24+00) exhibits broadband (0.2 to 10 Hz) amplification relative to the bedrock reference site JLDW, with the greatest amplification occurring in the 0.3 to 1.0 Hz range. JLD2 exhibits limited amplification between 1 and 4 Hz relative to JLDW, but the low-frequency (< 1.0 Hz) spectral ratio is near unity. The spectral ratio estimates from this data set are preferred over those obtained using the RefTek instrumentation because of the greater recording fidelity achieved. These spectral ratio estimates are therefore assumed to best characterize weak-motion site response on the north dike from the available data set.

difference in phase between JLDW and JLD2 or JLD3), and also the average relative phase response. The generated weak-motion impulse response functions are neither causal nor minimum phase.

For this study, the relative phase spectrum is used primarily as a means to generate a suitable weak-motion impulse response function, and little physical meaning is attached. Given the 1000-ft (300 m) separation between JLDW and JLD2, and the 2400-ft (730 m) separation between JLDW and JLD3, the observed waveforms are expected to exhibit little coherency at high frequencies. The only correction made for propagation delay for phases traveling between the two stations was to line up the time windows on the picked S-wave arrival time at each site. Because the relative phases exhibit a common trend only for the lowest frequencies, we did not attach much significance to the average of the phase responses from multiple events. The average phase response tended towards an arbitrary value for frequencies greater than about 1 Hz, which results in a tendency to compress the impulse response function in time (with corresponding magnification of amplitude). This effect is greater at JLD3, where substantial low-frequency energy arrives in later phases, than at JLD2.

5.3.1 Impulse Response Functions for JLD2 and JLD3. Figure 5-11A shows the unwrapped relative phase spectra for seven selected events recorded at JLD2, as well as the average relative phase spectrum for all 24 events used to compute the amplitude spectral ratio. Figure 5-11B shows the corresponding impulse response functions generated by using the average phase, and several of the single-event phases. The impulse response function using the average phase is more compressed in time than if single-event phases are used.

By construction, the amplitude spectral content of the impulse response functions exactly matches the observed spectral ratios; only the phase is variable. In choosing a specific relative phase spectra to develop impulse response functions, our goal is to produce qualitative agreement with the characteristics observed in the weak-motion data. For JLD2, the average phase provides a slight amplification and minimal prolonging of duration, which is observed in the weak-motion waveforms. Figure 5-12 shows the result of convolving the average and single-event impulse response functions with the Tabas E-W record (discussed in Section 6.6). For acceleration, each of the impulse functions reproduces the slight amplification observed in the weak-motion data,
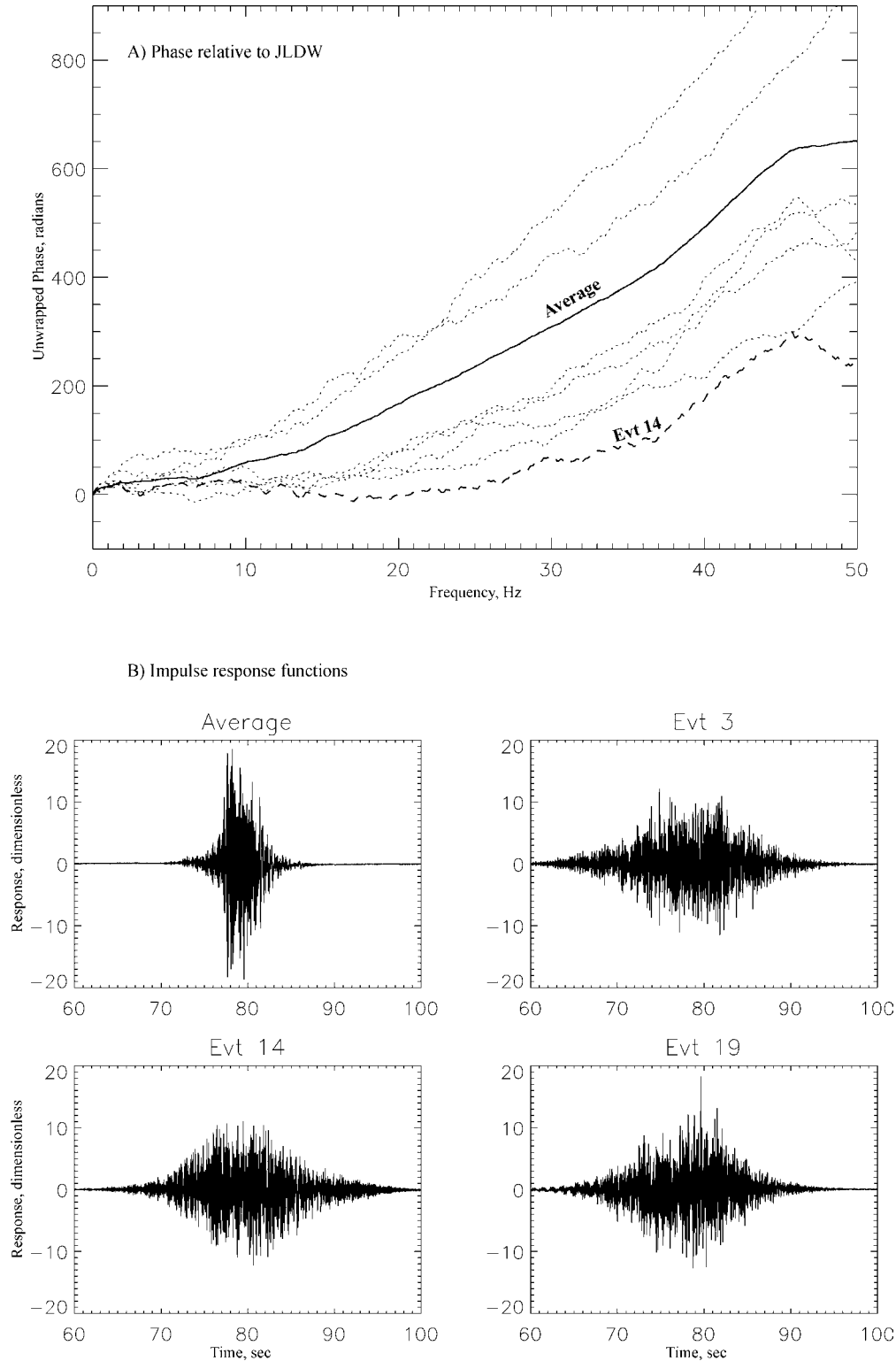
Figure 5-11: (A) Unwrapped phase at JLD2 relative to JLDW for 7 representative earthquakes. (B) Impulse response functions constructed from the average spectral ratio, and from individual or average relative phases. The non-causal part of the response is indicated by points prior to 81.92 seconds.
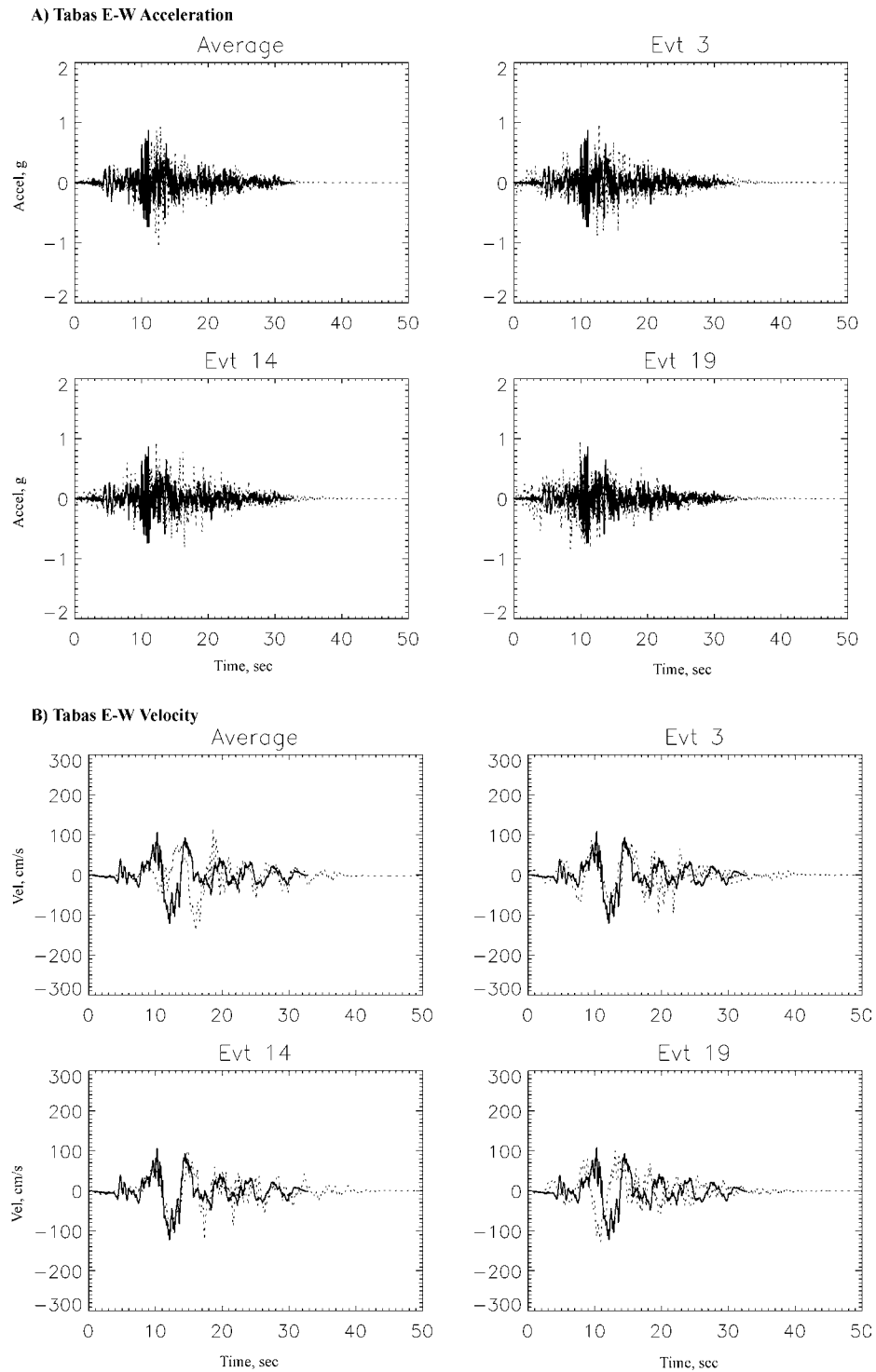
A) Tabas E-W Acceleration

B) Tabas E-W Velocity

Figure 5-12: Tabas E-W acceleration and velocity waveforms (solid lines) convolved with several realizations of the JLD2 weak-motion impulse response functions (dashed lines). For acceleration, each of the impulse functions reproduces the slight amplification observed in the weak-motion data, with minimal prolonging of duration. In contrast, the single-event impulse-response functions tend to slightly increase the duration of the velocity waveform. The impulse response function based on the average phase is therefore selected for JLD2

with minimal prolonging of duration. In contrast, the single-event impulse-response functions tend to slightly increase the duration of the velocity waveform. We have therefore selected the impulse response function determined from the average relative phase spectra to best represent JLD2.

The main characteristics observed in the site response data for JLD3 are amplification and prolonging of durations for frequencies between 0.2 and 1 Hz. Figure 5-13A shows the unwrapped relative phase spectra for the same set of seven events, but recorded at JLD3. Figure 5-13B shows the corresponding impulse response functions generated by using the average phase and three single-event phases. Again, our goal is to select a phase that produces the best qualitative agreement with the observed weak motion data. For JLD3, the resulting impulse response function needs to amplify and extended the duration of the low-frequency components of the convolved input waveform. For JLD3, the average phase produces an impulse response function that is too compressed in time relative to those determined for the single-event phases, and relative to the observed data. The relative phase spectrum from the earthquake labeled "Evt 14" appears to provide better qualitative agreement with the observed weak motion data. Figure 5-14 shows the result of convolving the average and single-event impulse response functions determined for JLD3 with the Tabas E-W record. For acceleration, the average phase produces the strongest amplification but little prolonging of duration. In contrast, the single-event impulse-response function for Evt-14 produced the greatest increase in the duration of the velocity waveform.   The relative phase spectrum for this event is labeled on Figure 5-13, and is seen to have the greatest delay of the phases considered. We have therefore selected the impulse response function determined from the relative phase spectra from Event 14 to best represent JLD3.

   5.3.2   Bedrock Motions with Weak-Motion Site Response Included.   Figure   5-15 shows the result of convolving selected design bedrock ground motions with the weak-motion impulse response function for JLD2. The three bedrock motions (described in Chapter 6) represent a range of realizations for the Teton Fault design ground motions. As with the observed weak-motion data, the ground motions convolved with the JLD2 site response have essentially the same duration as the input motions, and exhibit only minor high-frequency amplification.
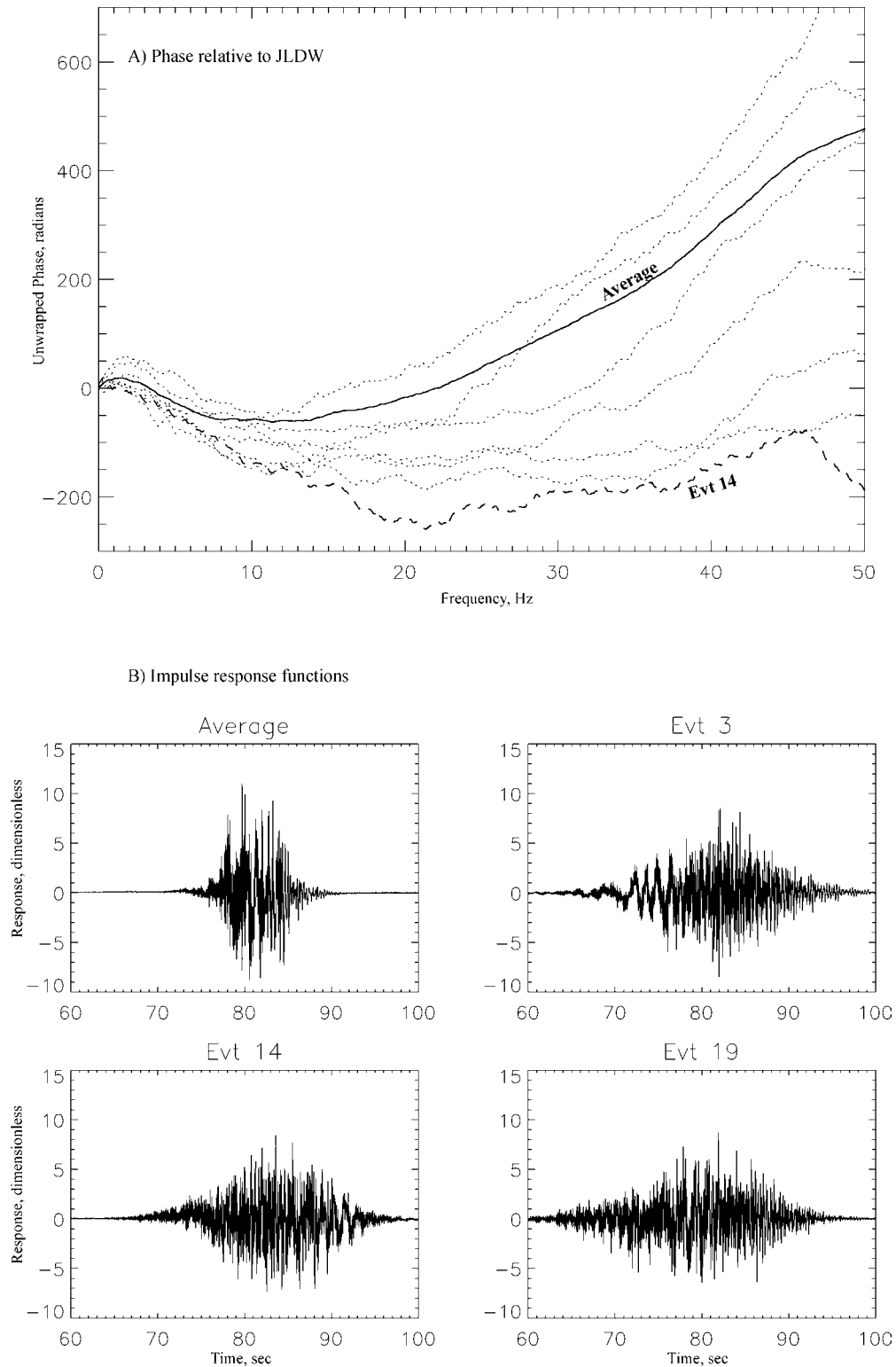
Figure 5-13: (A) Unwrapped phase at JLD3 relative to JLDW for 7 representative earthquakes. (B) Impulse response functions constructed from the average spectral ratio, and from individual or average relative phases. The non-causal part of the response is indicated by points prior to 81.92 seconds.
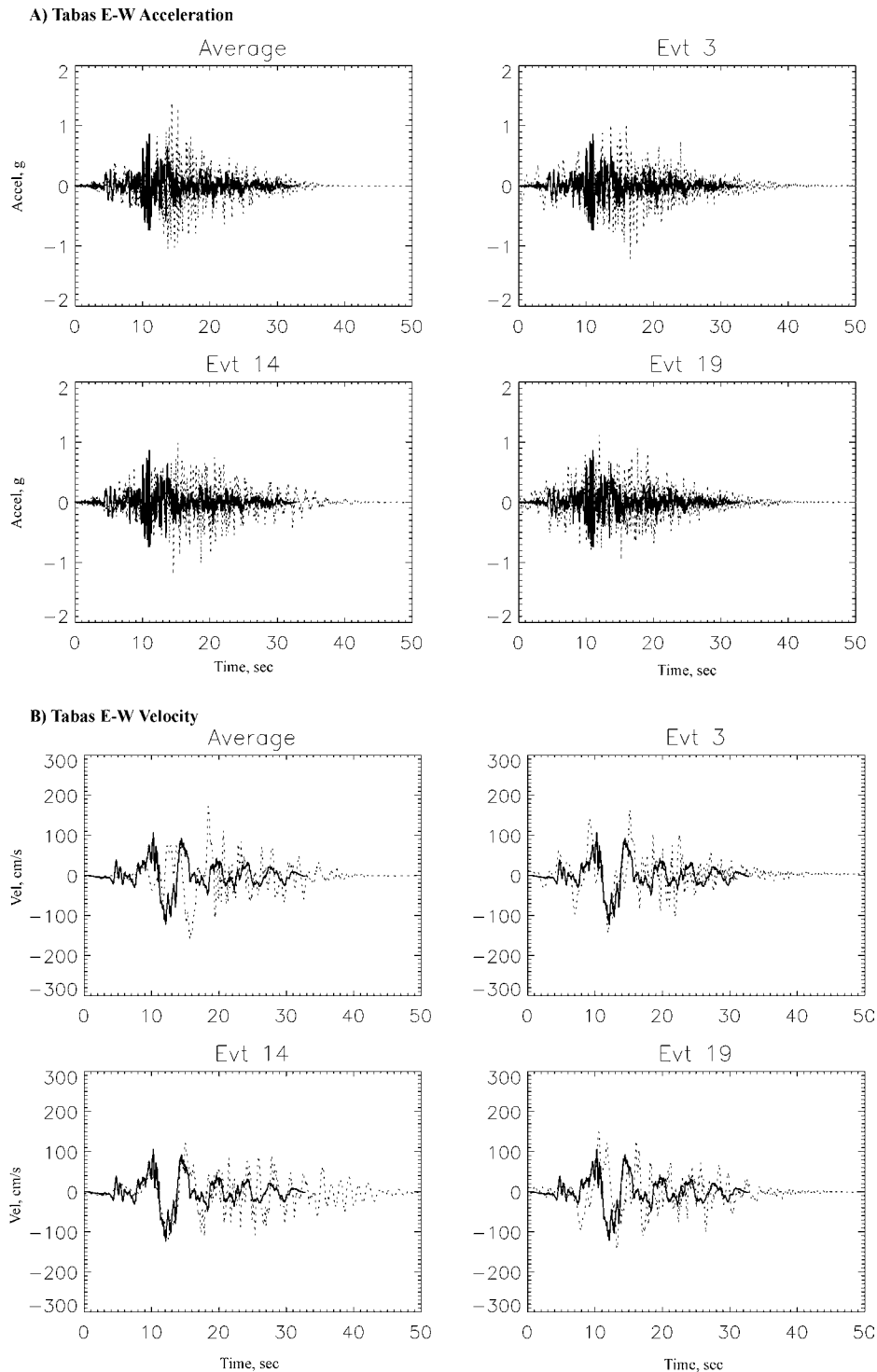
A) Tabas E-W Acceleration

B) Tabas E-W Velocity

Figure 5-14: Tabas E-W acceleration and velocity waveforms (solid) convolved with several realizations of the JLD3 weak-motion impulse response functions (dashed). As discussed in the text, the impulse response constructed from the average of the relative phase spectra underpredicts duration and overpredicts amplification. The impulse response function obtained from the relative phase spectrum for Event 14 provides better agreement with the prolonged durations observed in the weak-motion data

The ground motion simulations for JLD2 shown in Figure 5-15 are intended to be used as design ground motions at stations 12+00 and less. Significant non-linear behavior of the soils at JLD2 is not expected. The underlying soil column consists of glacial drift, gravels, tuffs and ash which have much higher shear wave velocities than are seen in the fluviolacustrine sands and gravels further out on the north dike. The observed weak-motion response at JLD2 is very similar to the bedrock reference site JLDW. Thus the simulations presented in Figure 5-15 can be used for design loadings at stations 12+00 and less, including the concrete section and south dike.
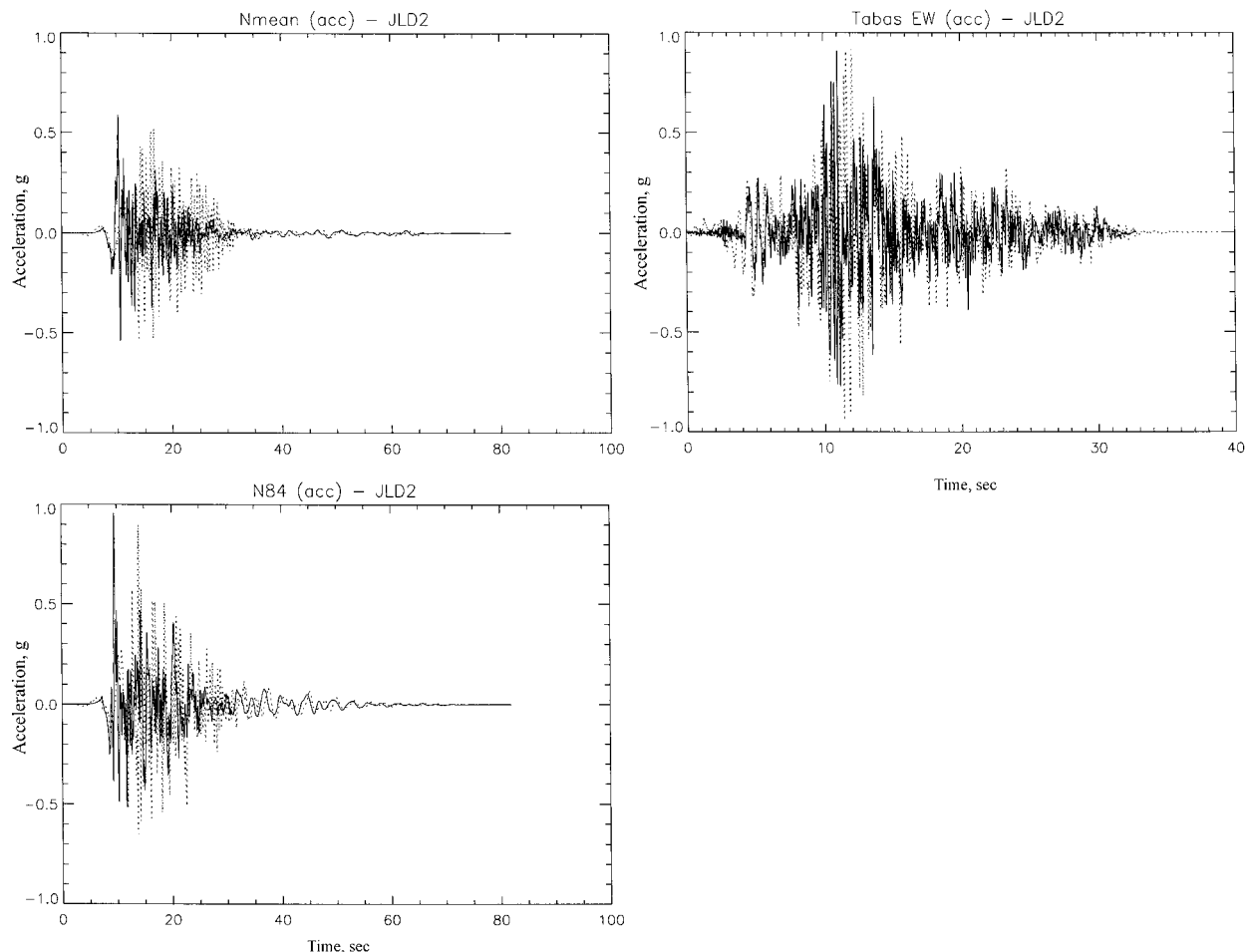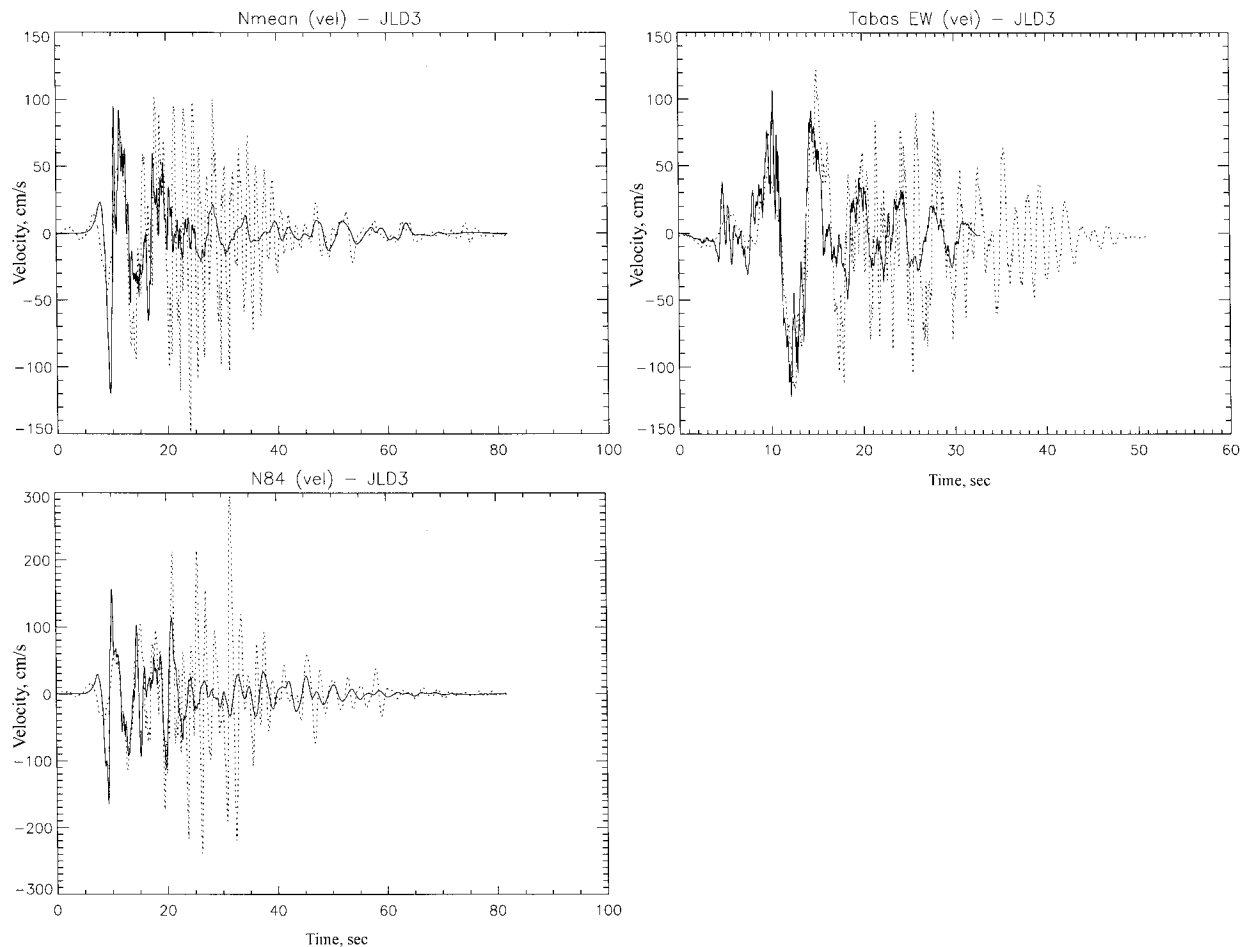

Figure 5-15: Bedrock input motions (solid lines), and bedrock motions convolved with JLD2 weak-motion response (dotted lines). Because the soil column underlying JLD2 appears to consist mostly of glacial drift and gravels, has reasonably high shear wave velocities, and has a low-frequency response that is not amplified relative to the bedrock reference site JLDW, a substantial nonlinear response to strong shaking is not expected. The bedrock motions convolved with the JLD2 site response should be used for design loadings at stations 13+00 and less.

Figure 5-16 shows the result of convolving the selected design bedrock motions with the JLD3 weak-motion site response. Velocity waveforms are shown. As expected, the convolved ground motions reproduce the longer durations observed in the weak motion data (though the amount depends on the input motion). By construction, the Fourier amplitude spectra of the convolved motions are simply the product of the input motion amplitude spectra and the average spectral ratio for JLD3 relative to JLDW. While the convolved waveforms shown on Figure 5-16 reproduce the observed effect of prolonged durations, the full non-linear site response needed for engineering analysis is not included.

Figure 5-16: Bedrock input motions (solid lines), and bedrock motions convolved with JLD3 weak-motion response (dotted lines). The weak-motion response does not include the non-linear soil response expected during strong ground shaking

When subjected to strong ground motions, the soils at station 24+00 (JLD3) are expected to behave non-linearly. Poorly consolidated, potentially liquefiable fluviolacustrine sands and gravels with shear velocities as low as 300 ft/s (100 m/s) underlie much of the north dike. The bedrock motions convolved with the JLD3 weak-motion response do not account for non-linear soil behavior, which must be accounted for separately. The observed site response at JLD3 is consistent with the 2-D and 3-D response of a sedimentary basin, and likely results from the generation of surface waves, converted phases, and interface waves. These effects are not accounted for by 1-D models. However, available computer codes for estimating non-linear soil behavior are based on propagating an incident body wave (typically a horizontally polarized S wave) through a 1-D soil column. In order to permit use of 1-D non-linear soil response computer codes, while preserving the observed 2-D and 3-D effects of prolonged duration and long-period amplification, we will modify (in subsequent sections) the weak-motion impulse response for JLD3 to approximately account for the linear response of the soil column from a reference depth, and the free surface effect. The modified impulse response is then convolved with the simulated bedrock motions and input to the non-linear soil response codes at the selected reference depth. There is considerable uncertainty in this method because the reduction of the convolved surface motions to a reference depth cannot accurately account for the depth dependency of surface waves and converted phases.

As discussed in section 5.2, we don't know the precise location of the transition in site response observed between stations 13+00 (JLD2) and 24+00 (JLD3-5). Based on drilling and geophysical logging, we would expect the transition to be near 14+00, although this is not certain. Thus engineering analyses for stations at 14+00 or greater should use the JLD3 response, and stations less than 14+00 should use the JLD2 response.

We have constructed velocity and acceleration response spectra for each of the selected bedrock motions and for the motions convolved with the weak motion site response. These provide a further indication of the effects of the weak motion site response. Figure 5-17 shows the bedrock input motions convolved with the JLD2 site response. Absolute acceleration response spectra are provided. These response spectra for JLD2 may be used for engineering analyses at stations 13+00 or less, including the concrete interface structure, spillway and bridge.
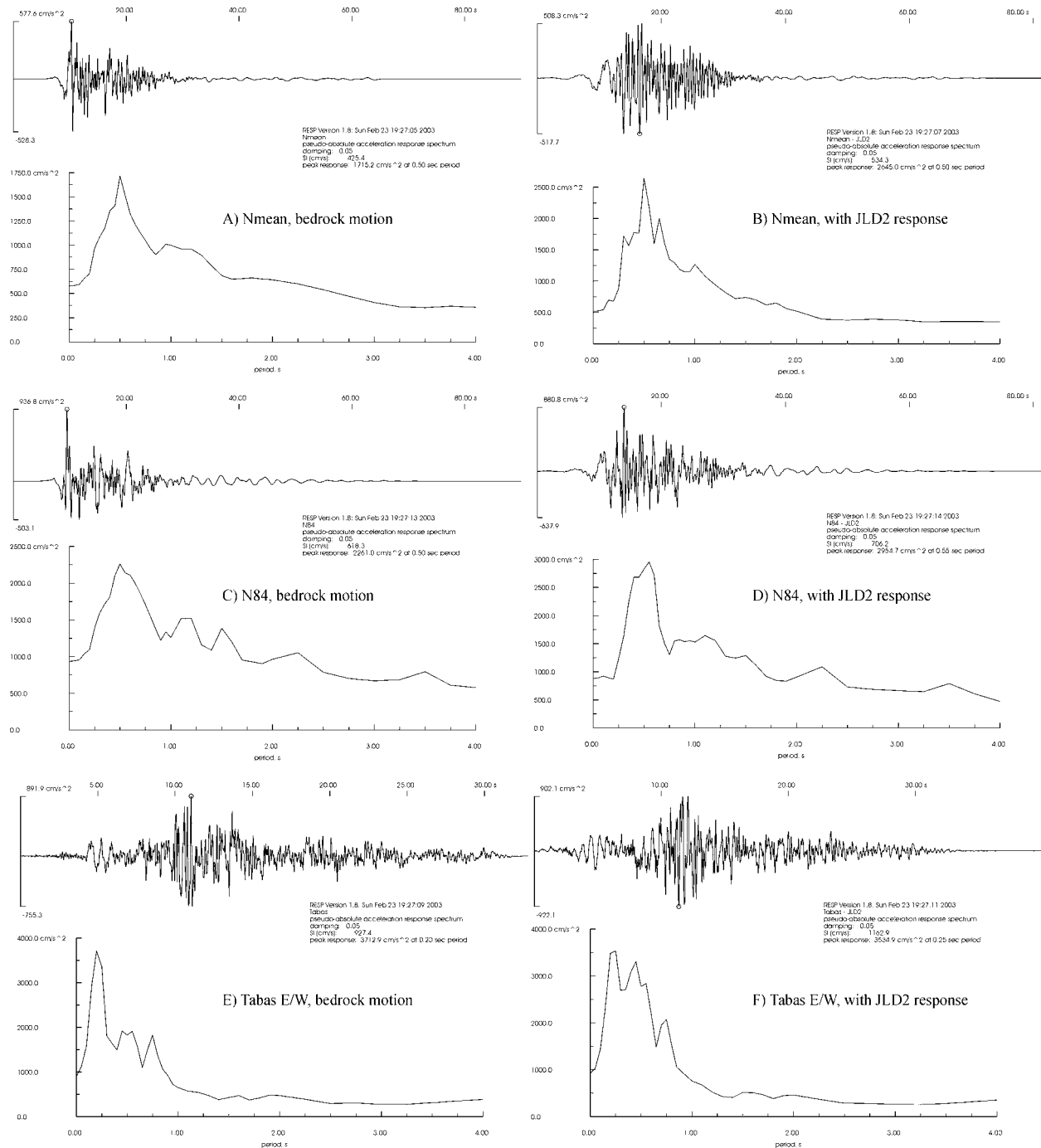
Figure 5-17: Bedrock input motions (left), and motions convolved with JLD2 weak-motion site response (right). Three bedrock motions (described in Chapter 6) representing a range of realizations for the Teton Fault design ground motions are shown: N-mean, N-84, and Tabas-E/W.   Absolute acceleration response spectra for 5% damping are shown below each time history. The bedrock motions convolved with the weak motion JLD2 site response may be used for design loadings at stations 13+00 or less. A substantial non-linear response to strong shaking is not expected at these locations

Figure 5-18 shows pseudo-relative velocity response spectra for the bedrock motions convolved with the JLD3 site response. These response spectra are applicable at stations 14+00 and greater. However, because the convolved motions at JLD3 shown in Figure 5-18 do not include non-linear soil effects, these motions must be further modified to include non-linear soil behavior before they can be used in engineering analyses. This is done in the following sections.

5.4 2D Finite-Difference Site Response Modeling

Borehole recordings of ground motions in the soil section of Jackson Lake Dam are not available. Consequently, it is necessary to infer the properties of subsurface ground motions using theoretical methods with available geophysical information about the site conditions. The geological and geophysical data provide important information about the variation of materials and seismic velocities along the axis of the dam. However, very little information is available about the geometry and geophysical properties of soils upstream, downstream, and north of Jackson Lake Dam. Since information about the 3D geometry and velocity of the glacial scour basin is not available, 2D finite-difference methods are used to obtain a physical understanding of the likely composition of seismic waves that produce the amplification and prolonged durations observed at JLD3-7. The goal is to obtain sufficient understanding of wave propagation in the very-low-velocity soils to construct realistic input ground motion scenarios at sufficient depth to allow calculation of nonlinear soil responses using 1D approximations.

5.4.1 Previous Work. Lomnitz et al. (1999) provided theoretical evidence and ground motion recordings from Mexico City that showed that long duration monochromatic ground motions may be produced in basins that have low shear-wave velocities (0.1 to 0.2 km/s) and saturated sediments. However, Lomnitz et al. (1999) did not calculate synthetic seismograms to demonstrate the physical existence of their postulated PR mode. O'Connell and Ake (2003) performed 2D finite difference investigations of the existence of Lomnitz et al.'s (1999) PR mode and their results are reproduced here since the PR mode may be one way to explain the observed long duration soil ground motions described in Section 5.2 To test the ability of such a long duration mode to persist in a basin with strong intrinsic attenuation, a model of a small (0.3 km wide and 0.1 km deep), glacial scour is embedded in a 2D model with slightly higher shallow velocities outside the basin and higher velocities at depth (Figure 5-19a). Values of Q=10 were
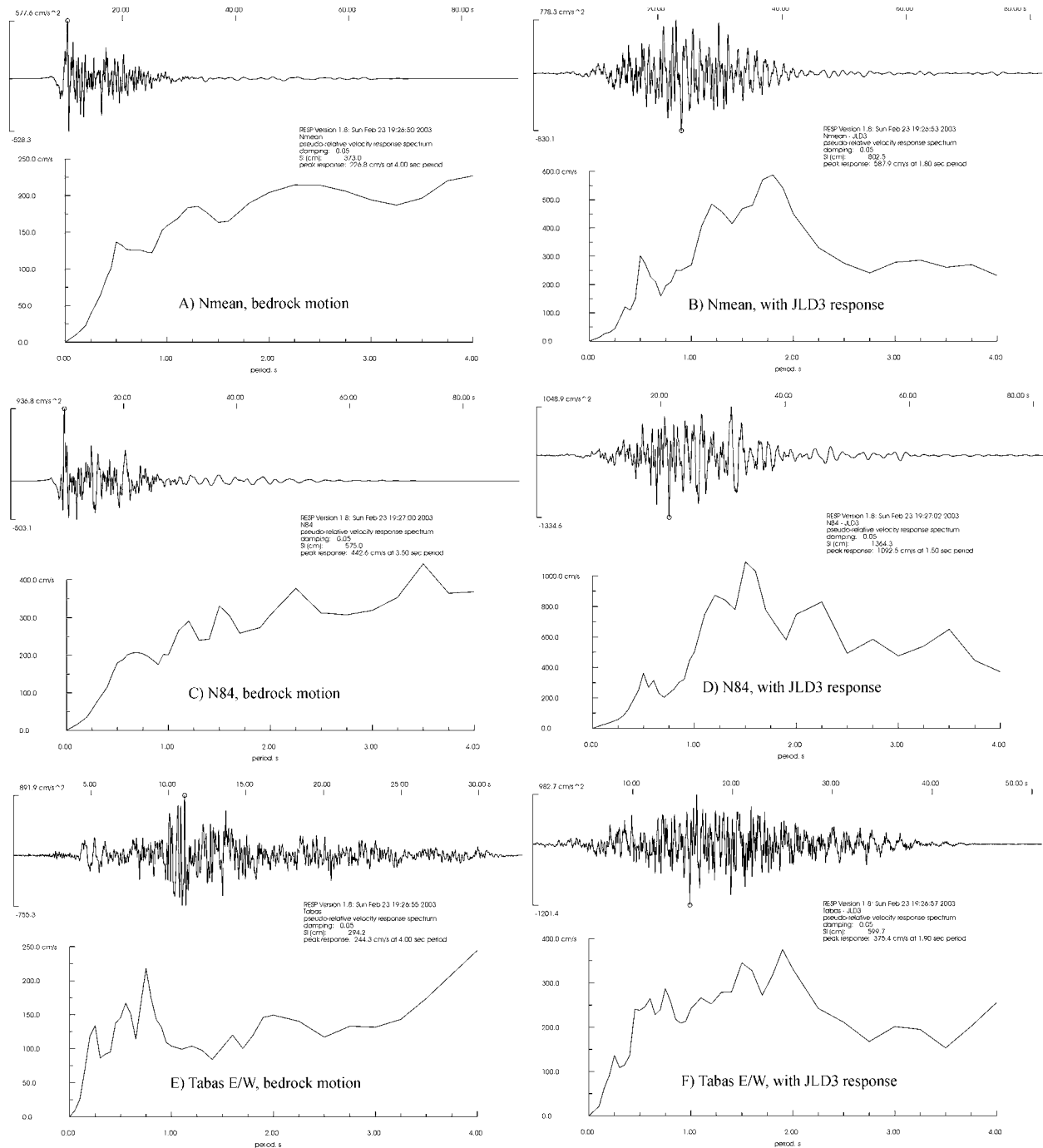
Figure 5-18: Bedrock input motions (left), and motions convolved with JLD3 weak-motion site response (right). Three bedrock motions (described in Chapter 6) representing a range of realizations for the Teton Fault design ground motions are shown: N-mean, N-84, and Tabas-E/W.   Pseudo-relative velocity response spectra at 5% damping are shown below each time history. The bedrock motions convolved with the weak motion JLD3 site are intended to be used at stations 14+00 and greater with a suitable correction for non-linear soil response. A substantial non-linear response to strong shaking is expected at these locations, and the weak-motion surface response provided here must be corrected for input to the base of the soil column. That correction is provided in subsequent sections

used to simulate high-intrinsic attenuation in the near-surface, low-velocity materials. Compressional wave velocities were set to water velocities for the lowest velocity materials. The 2D version of the elastic finite-difference program E3D (Larsen and Grieger, 1998), which includes viscoelastic capabilities implemented using the approach of Robertsson et al. (1994), was used to calculate the seismic response of a *SV* plane-wave incident at 5° from vertical upon the basin with a total moment of 10^{20} dyne-cm. The numerical model was 8 km long and 5 km deep with attenuating boundaries to minimize spurious internal reflections. The source-time function was a differentiated 0.75 s-duration Gaussian pulse. The incident horizontal velocity response is shown at the bottom of Figure 5-19b.

Constructive interference at the center of the basin produces maximum amplitudes that persist for ~7 s and a slow amplitude decay lasting about 20 s (Figure 5-19b). Sites offset from the center of the basin experienced long-duration monochromatic horizontal motions with slowly decaying amplitudes that persisted to the maximum calculation time of 60 s. The long duration response are produced by the interface modes propagating horizontally back and forth across the basin as they reflect off the vertical boundaries at the basin edges (Figure 5-19c). Ground motion responses similar to the top time history in Figure 5-19b were observed for earthquakes recorded by stations JLD3, JLD4, JLD5, JLD6, and JLD7 (Figures 5-4 and 5-5). The simulation shows that this mode can persist for long durations with little effective attenuation of the mode, even though intrinsic S-wave attenuation is high. However, the schematic velocity model has limited applicability to Jackson Lake Dam. Consequently, a velocity model more consistent with the geophysical and geological data from Jackson Lake Dam is used in the next section to simulate responses in the low-velocity glacial scour.

5.4.2 Site-Specific Model. The available information about the variations of velocities in the glacial scour and the overall geometry of the glacial scour are limited. The southern extent of the glacial scour low-velocity basin is well constrained by geophysical and geological information. The drill logs provide good constraints on the depth to the ~1 km/s till from the south end of the glacial scour to the northern end of the embankment. In contrast the northern limit of the glacial scour low-velocity basin is unknown. The northernmost and deepest drill log indicates that the glacial scour basin is still deepening at the northern end of the embankment. A velocity
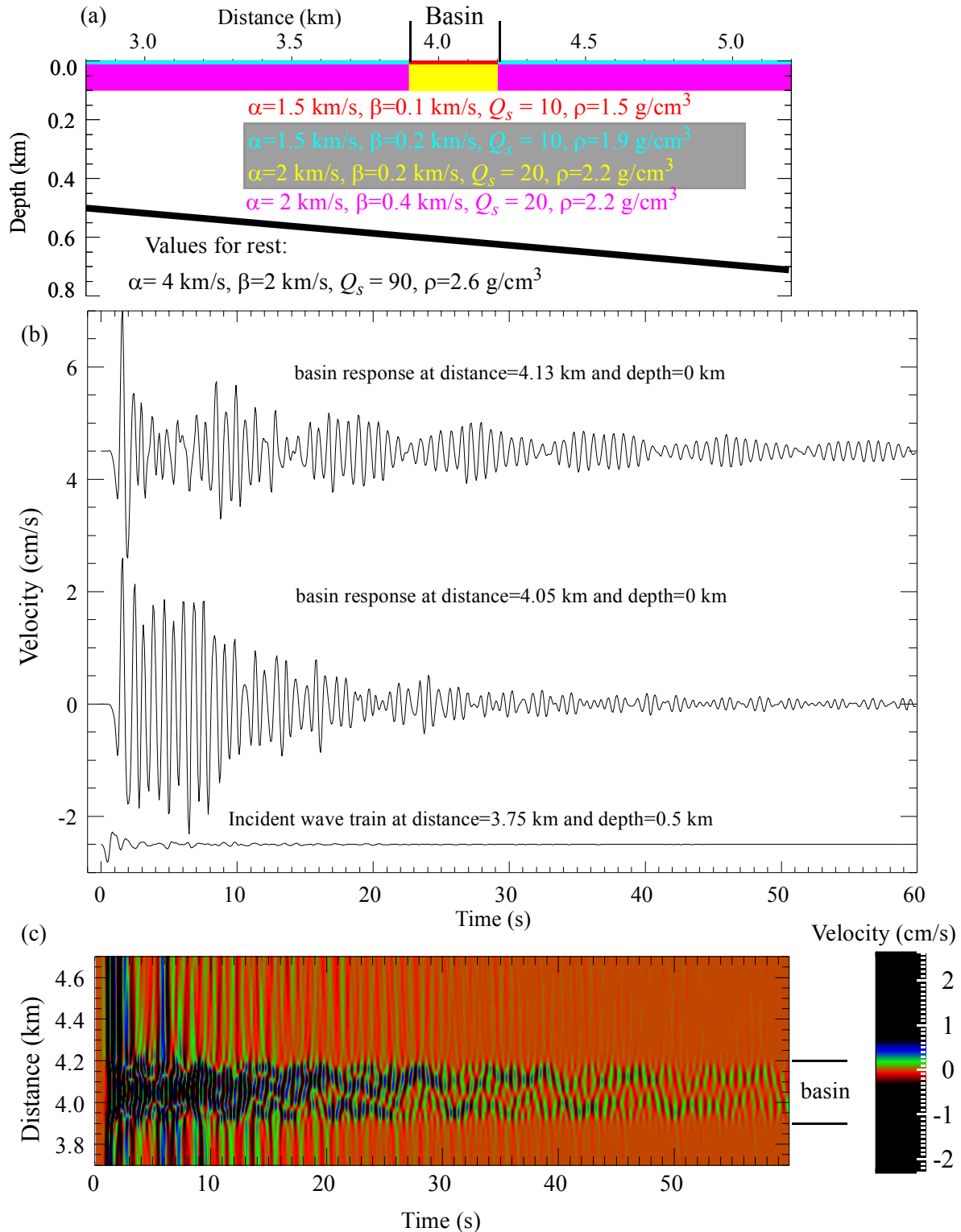
Figure 5-19: Simulation of Lomnitz et al.'s (1999) soil response. (a) Color-coded 2D material model. Thick line shows the incident SV plane wave. (b) Incident waveform at a depth of 0.5 km modified by internal reverberations is shown at the bottom, with two surface waveforms from sites located within the basin as labeled shown above. (c) Color-coded horizontal velocity time histories for surface sites located at distances from 3.7 km to 4.7 km.

model was constructed to produce a glacial scour basin at least as wide as permitted by the available observations (Figure 5-20); the actual glacial scour low-velocity basin may be significantly wider.

The lateral continuity of velocity discontinuities within the soils of the glacial scour are unknown. The approach used here was to minimize strong velocity discontinuities in depth to the two sharpest first-order velocity discontinuities (~27 m depth) and the interface with the underlying ~1 km/s S-wave-velocity till, and to use smooth velocity gradients for all other velocity changes (Figure 5-21). The premise is that if even this overly smooth velocity model produces long durations, it would be straightforward to identify the origins and characteristics of long duration waves. Since weak-motion attenuation of the soils may be very large, Qs was set to 5 at the surface and increased with S-wave velocity as show in Figure 5-22. The same 2D finite-difference approach used in Section 5.4.1 was used to model glacial scour responses at the surface and at depths of 0.1, 0.2, 0.3, 0.4, and 0.5 km as shown in Figure 5-20. A plane SV-wave inclined 5° from vertical incidence was input into the 2D finite-difference calculation as shown in Figure 5-20. The model was 8 km long and 5 km deep to minimize boundary reflections, the only significant boundary reflection is the primary reflection off the bottom of the model that produces a small S-wave arrival about 6 s following the first S-wave arrival. Since LVB-edge S-waves from the large-scale LVB are nearly ubiquitous at the dam, this reflected S-wave provides a somewhat more realistic input scenario than a single plane SV wave. The grid interval of 5 m and minimum S-wave velocity of 0.1 km/s limit the maximum frequency in the analysis to 4 Hz. The same time-differentiated Gaussian pulse used in Section 5.4.1 was used here.

The horizontal acceleration surface responses in Figure 5-23 show extended durations and amplification for sites located in the low-velocity glacial scour. The edge of the basin at 3 km produce the largest basin-edge wave amplitudes because the SV plane wave is incident toward the basin at 3 km. The dashed blue line shows that the early portion of the basin-edge waves are composed of S-waves with apparent velocities of ~0.2 km/s refracted below 25 m depth, followed by Rayleigh waves that end with a large-amplitude, broadband Airy phase (red dashed line is located at the end of the Airy phase at an apparent velocity of ~0.09 km/s, the minimum Rayleigh velocity for a surface velocity of 0.1 km/s). Within about 1 km of the basin-edge at 3 km, the
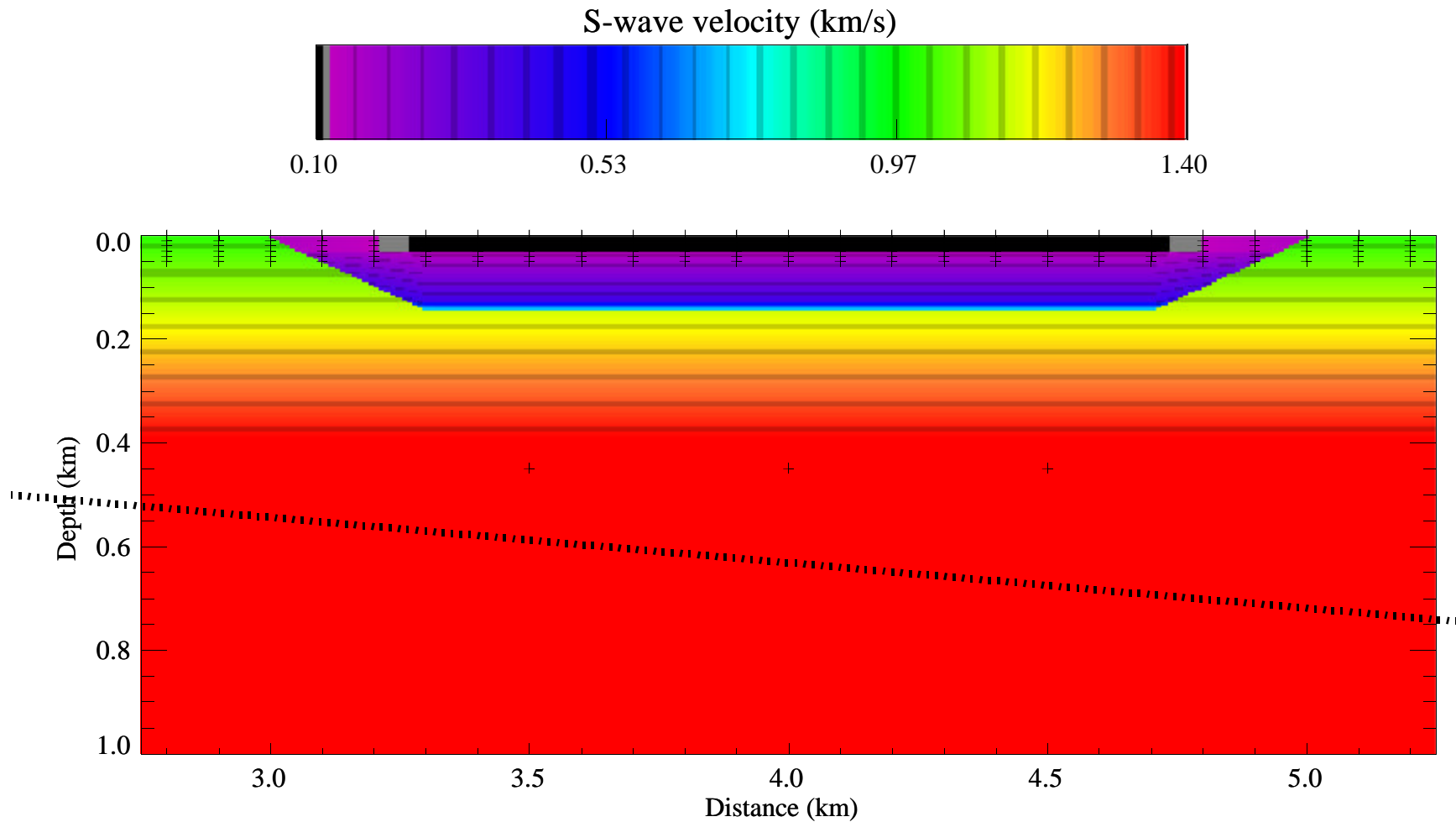
Figure 5-20: Simple 2D S-wave velocity model of the glacial scour basin beneath the dam.The dashed line represents the SV plane wave incident 5° from vertical. The plus symbols show where ground motion information was extracted from the model. The boundaries have 22.5° dips and horizontal velocity gradients which take the uniform 1D velocity variations in the flat-bottom portion of the very-low-velocity basin and linearly increase the velocities laterally toward the basin edges
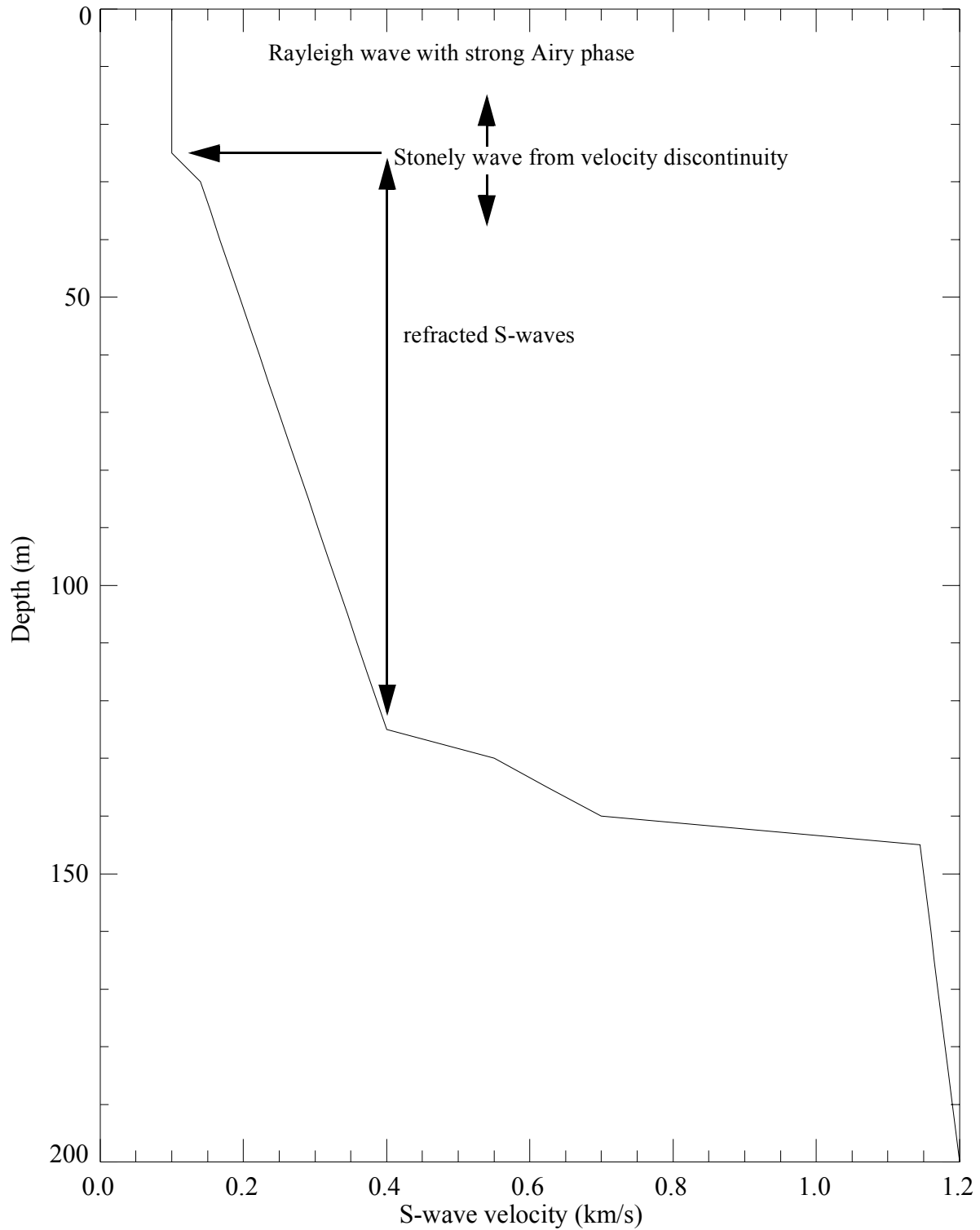
163

Figure 5-21: 1D S-wave velocity profile from the middle of the 2D glacial scour basin.The origin of different wave types is indicated schematically with depth; Fundamental Rayleigh waves in the top 25 m with associated large-amplitude Airy phase, Stonely waves radiated up and down from the velocity discontinuity at 25 m, and S-wave refracted by the velocity gradients below 25 m.
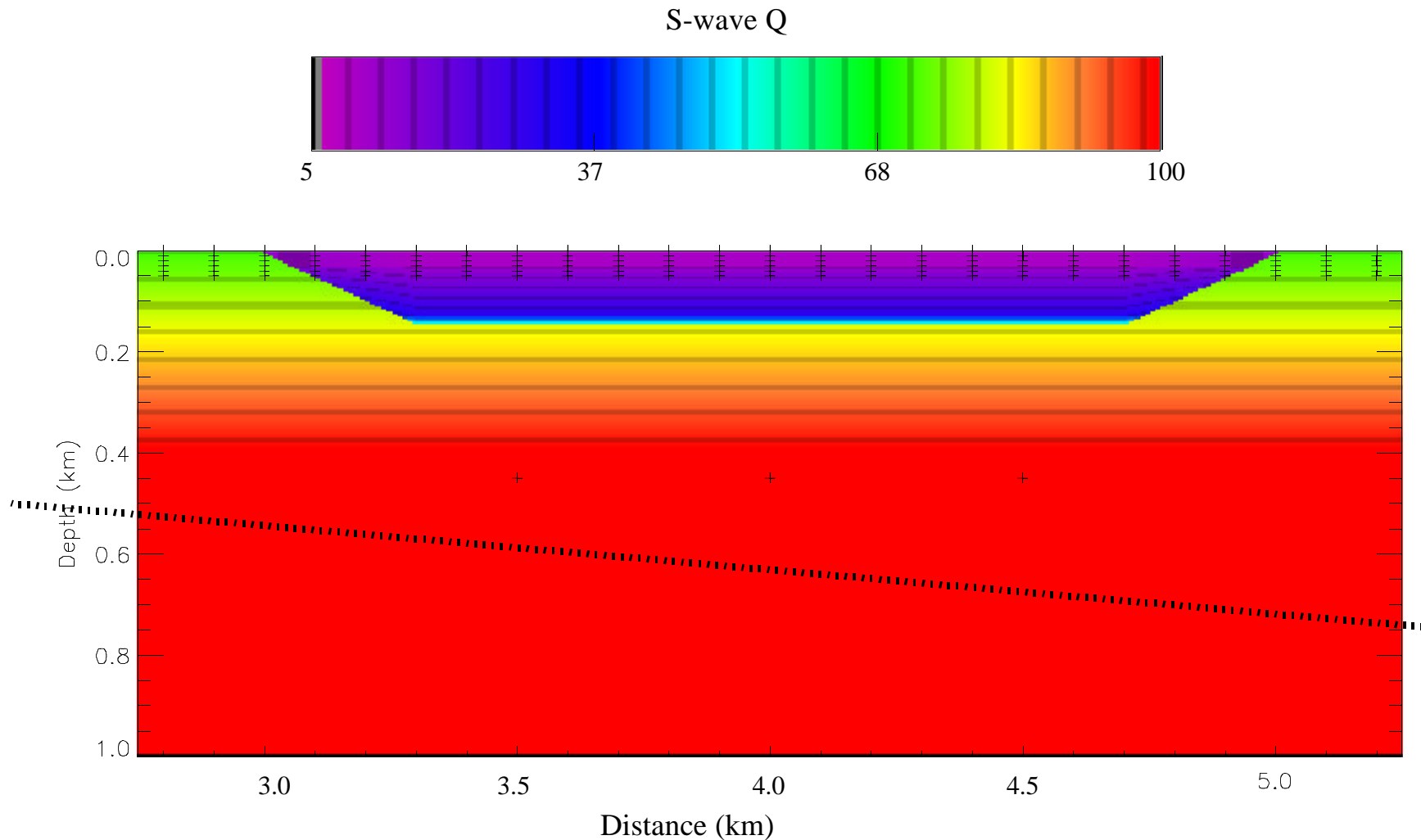
Figure 5-22: Simple 2D S-wave Qs model of the glacial scour basin beneath the dam. The dashed line represents the SV plane wave incident 5° from vertical. The plus symbols show where ground motion information was extracted from the model. The boundaries have 22.5° dips and horizontal Qs gradients which take the uniform 1D Q variations in the flat-bottom portion of the very-low-velocity basin and linearly increase Qs laterally toward the basin edges.
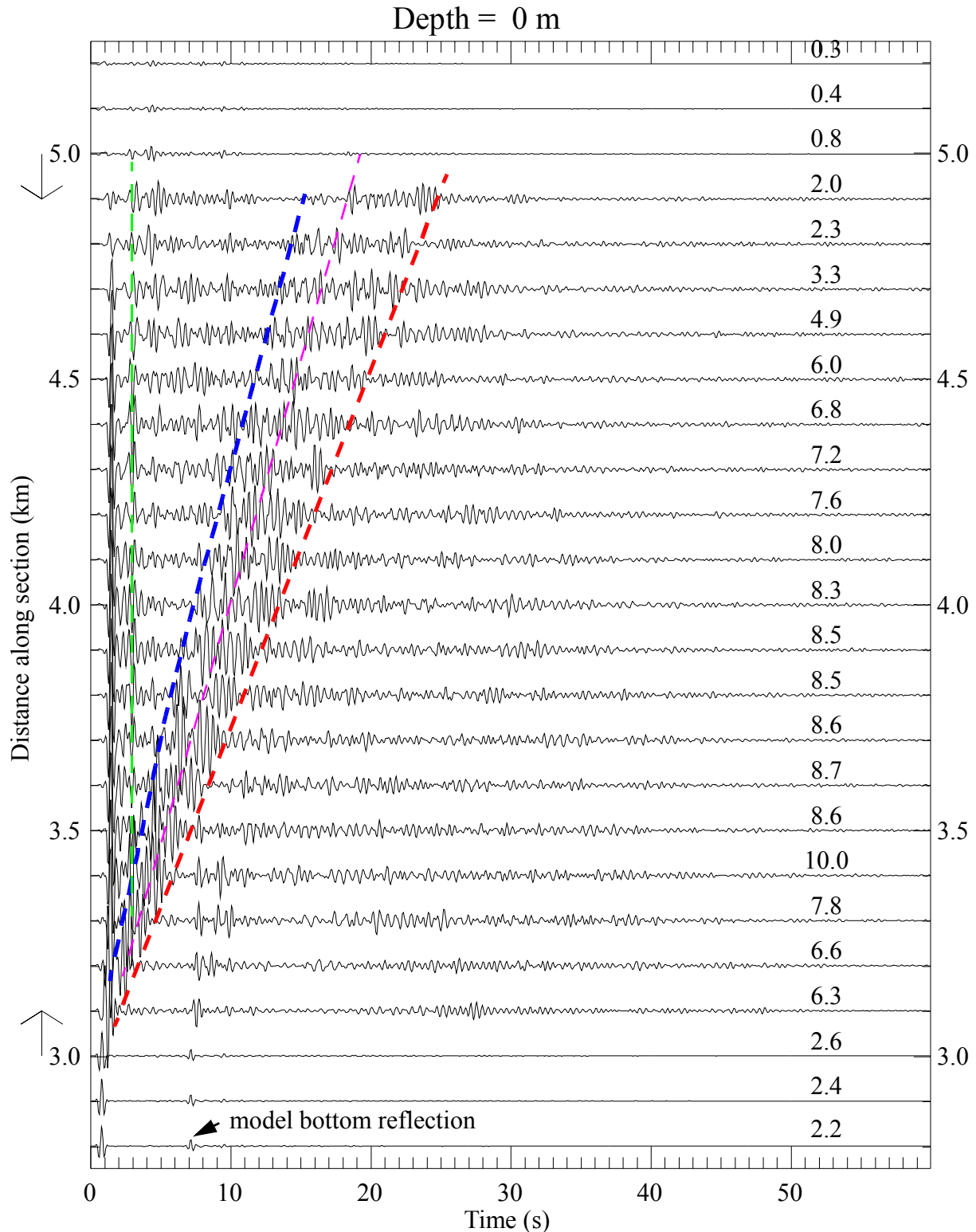
165

Depth = 0 m

Figure 5-23: Horizontal 2D finite-difference acceleration record section z = 0 m. Distances are as shown in Figure 5-22. Peak amplitudes are labels on the right normalized to a maximum value of 10 for all sites in the model. Low-velocity glacial scour sites are between the arrows on the left. Dashed red line shows the end of the basin-edge Airy phase. Dashed blue line is the basin-edge refracted S-wave. Dashed magenta line is the Stonely wave. Primary S-wave multiple is the dashed green line.

refracted S-wave has the largest amplitude. For distances > 4.4 km the low near-surface Qs properties and amplitude reduction past the S-wave triplication, leave the surface waves with the largest accelerations for the basin positions > 4.4 km (Figure 5-23). The fundamental mode Rayleigh Airy phase has the largest amplitudes at the far side of the basin, as surface wave amplitudes decay more slowly with distance. The basin edge waves contain substantial acceleration responses in the 1-4 Hz frequency range, as is expected for the S-waves, but the Rayleigh waves also have strong amplitudes in this frequency range. Figure 5-23 indicates that the portions of the southern glacial scour boundaries within several km of the dam are likely to produce substantial short-period acceleration responses along the embankment portion of the dam.

Figure 5-24 shows that horizontal acceleration durations decrease only slightly at 10 m depth and accelerations mostly decrease by about a factor of two, consistent with removing the free-surface effect. The refracted basin-edge S-waves are less attenuated since they don't have to propagate through as much shallow low Qs material. Also, as depth increases the multiple reflections from high-velocity basal till become less attenuated (compare Figures 5-23 to 5-24) because Qs increases with depth in the model. The Stonely wave arrival is the dominant later arrival after the multiple S-wave reflections for depths of 20 m (Figure 5-25) and 30 m (Figure 5-26) because these depths are closest to the velocity discontinuity at 25 m where the Stonely waves propagate with velocities of ~0.9 * Vs of the lowest velocity side of the interface. At depths of 40 m (Figure 5-27) and 50 m (Figure 5-28), the refracted S-waves and Stonely waves have comparable amplitudes (Figures 5-27 and 5-28), but the S-waves tend to retain higher frequencies, particularly closer to the basin margins, which are the secondary sources of these extended duration phases. It is clear that down to a depth of 50 m, the horizontal acceleration durations are not significantly less than the surface durations. In fact basin-edge refracted S-waves retain higher frequency acceleration responses relative to surface sites because deeper refracted S-waves are not subjected to the lowest Qs regions near the surface. Figures 5-23 to 5-28 demonstrate that it is necessary to use the observed durations at the surface stations, like JLD3, at depth to provide realistic duration input motions for nonlinear analyses of the soil responses. This is necessary because the 1D SH-propagator nonlinear codes SHAKE and NOAH will not generate the strong-amplitude S-waves or Stonely waves produced at the basin margins. Since the Stonely waves are
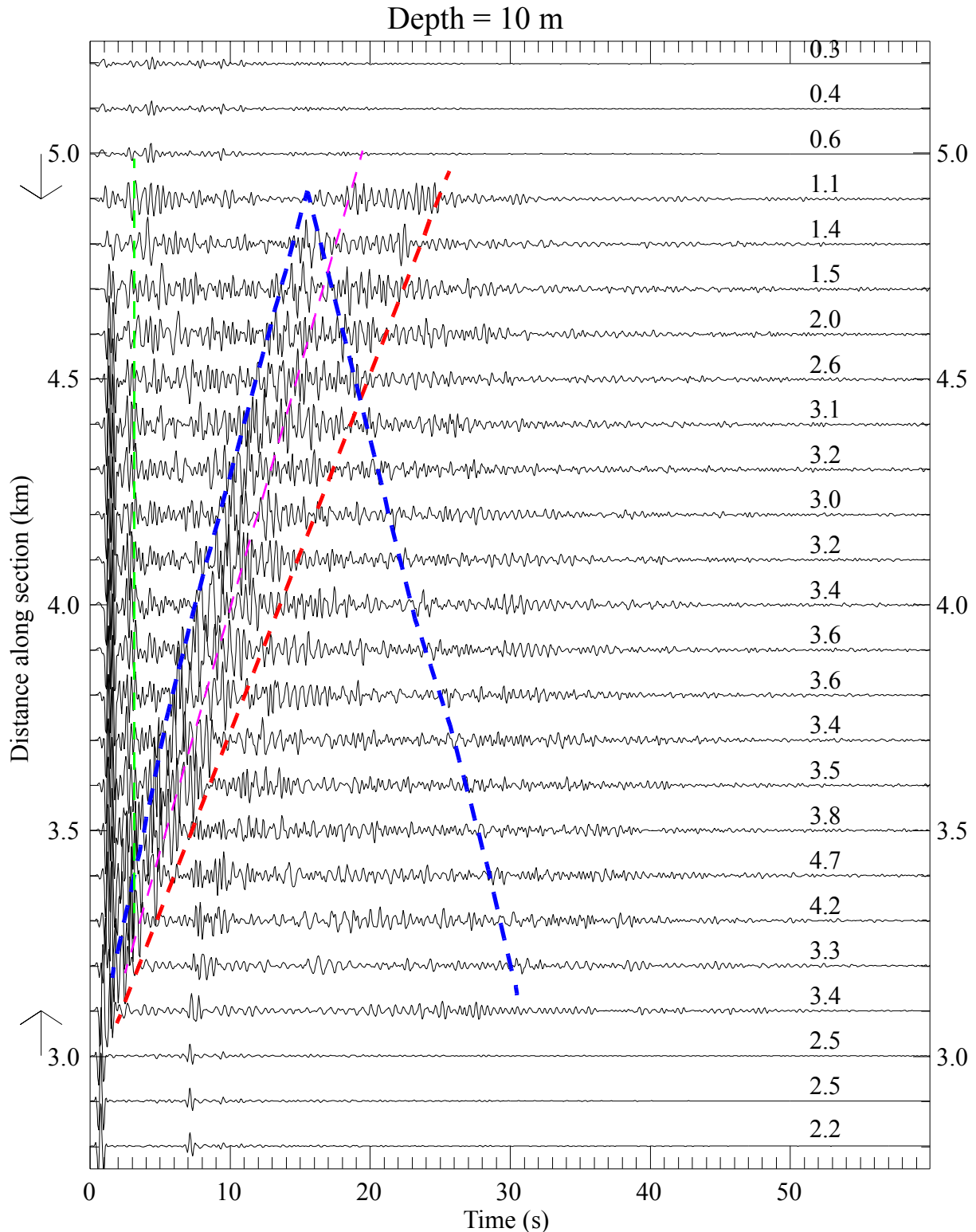
Depth = 10 m
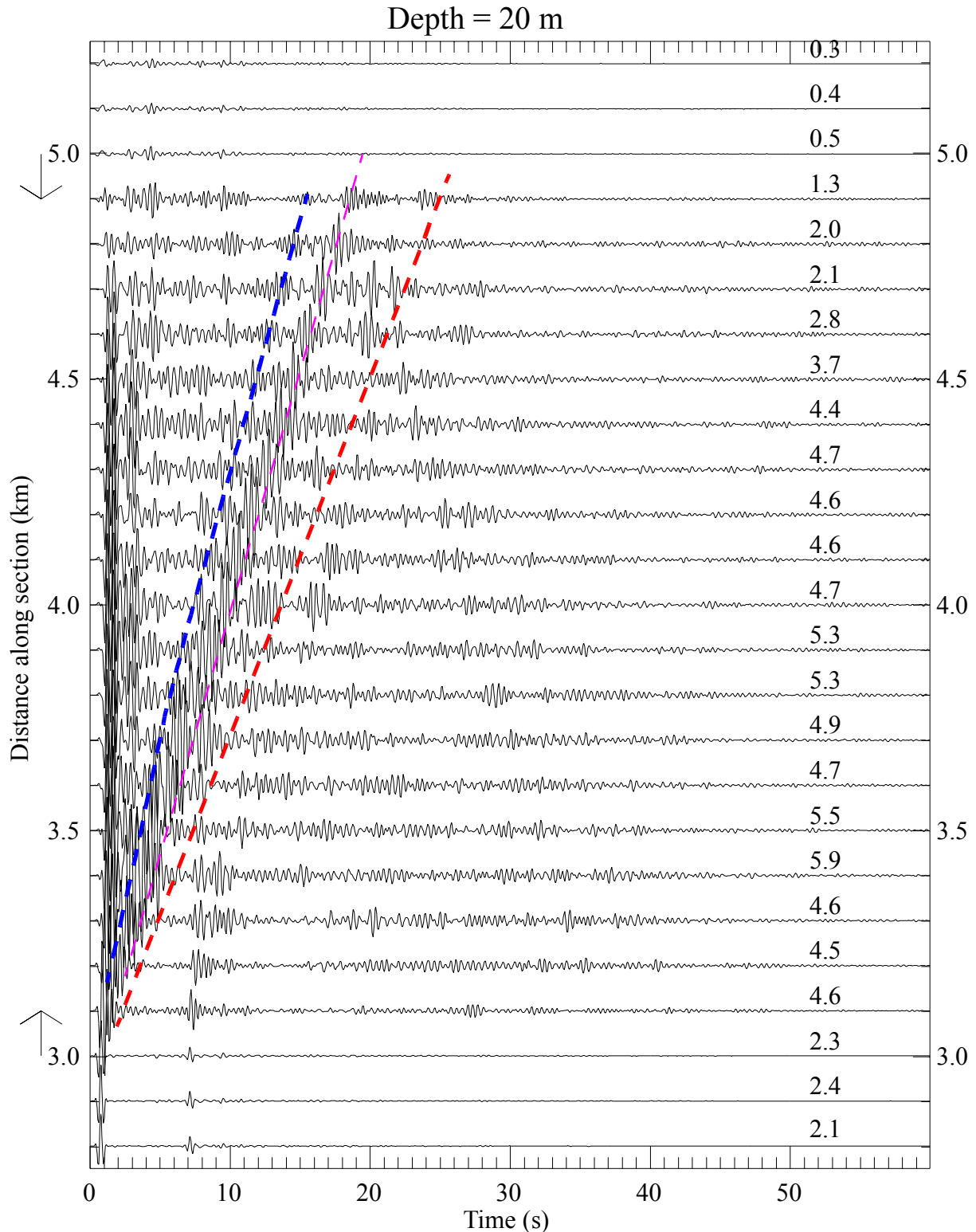

Figure 5-24: Horizontal 2D finite-difference acceleration record section z = 10 m. See Figure 5-22 for distance reference. Dashed red line shows the end of the basin-edge Airy phase. Dashed blue lines show the refracted basin-edge S-waves and surface waves, and their reflection back across the basin from the far edge. Primary S-wave multiple reflection from the ~1 km/s till is the dashed green line. The dashed magenta line shows the Stonely wave from the velocity discontinuity at 25 m depth.

Depth = 20 m

Figure 5-25: Horizontal 2D finite-difference acceleration record section z = 20 m. See Figure 5-22 for distance reference. Dashed red line shows the end of the basin-edge Airy phase. Dashed blue lines show the refracted basin-edge S-waves and surface waves, and their reflection back across the basin from the far edge. The dashed magenta line shows the Stonely wave from the velocity discontinuity at 25 m depth.
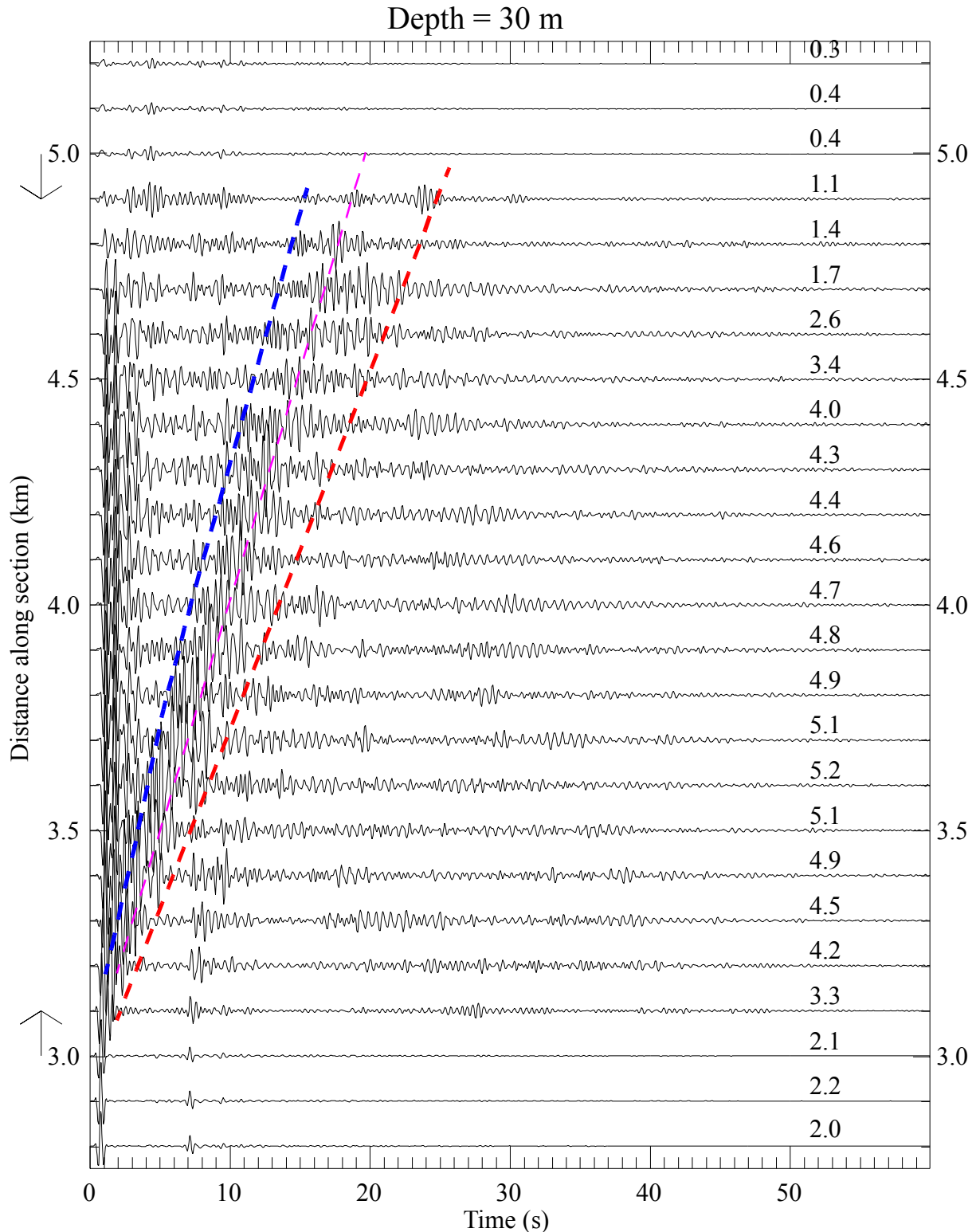
Depth = 30 m

Figure 5-26: Horizontal 2D finite-difference acceleration record section z = 30 m. See Figure 5-22 for distance reference. Dashed red line shows the end of the basin-edge Airy phase. Dashed blue lines show the refracted basin-edge S-waves and surface waves, and their reflection back across the basin from the far edge. The dashed magenta line shows the Stonely wave from the velocity discontinuity at 25 m depth.
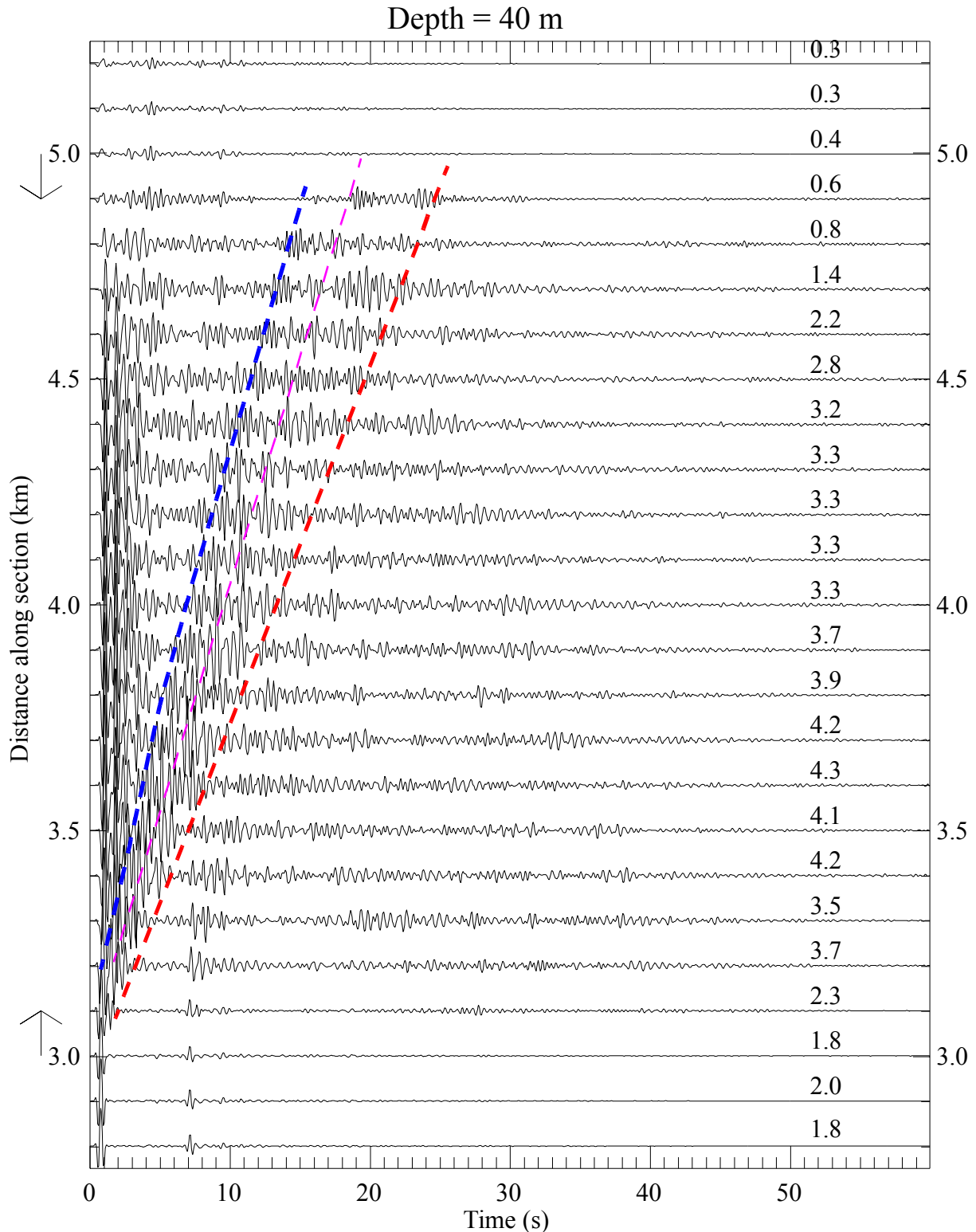
Depth = 40 m

Figure 5-27: Horizontal 2D finite-difference acceleration record section z = 40 m. See Figure 5-22 for distance reference. Dashed red line shows the end of the basin-edge Airy phase. Dashed blue lines show the refracted basin-edge S-waves and surface waves, and their reflection back across the basin from the far edge. The dashed magenta line shows the Stonely wave from the velocity discontinuity at 25 m depth.
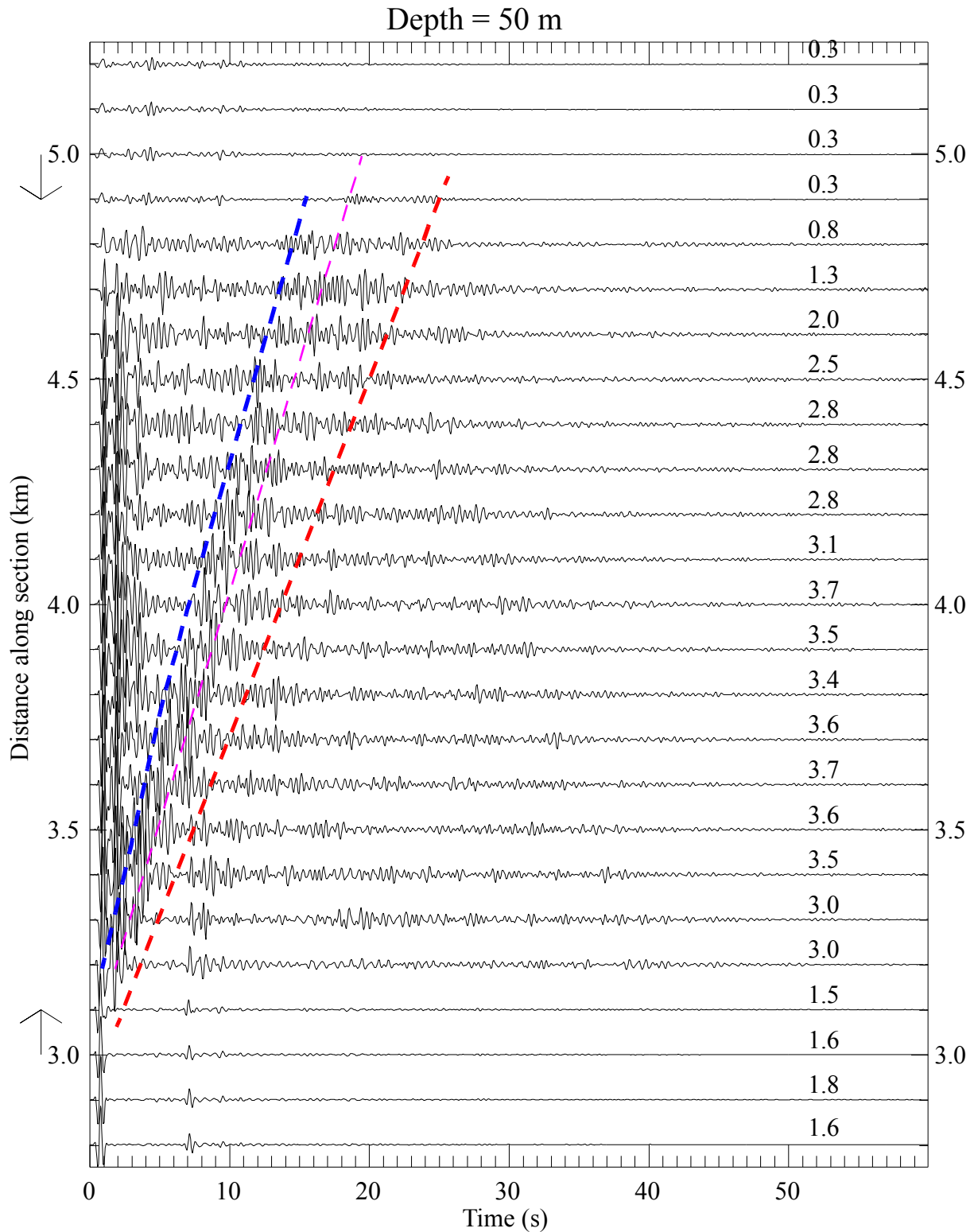
Depth = 50 m

Figure 5-28: Horizontal 2D finite-difference acceleration record section z = 50 m. See Figure 5-22 for
distance reference. Dashed red line shows the end of the basin-edge Airy phase. Dashed blue lines
show the refracted basin-edge S-waves and surface waves, and their reflection back across the basin
from the far edge. The dashed magenta line shows the Stonely wave from the velocity discontinuity at
25 m depth.

elliptically polarized, horizontal propagating, they are least compatible with the SH body wave assumptions of SHAKE and NOAH.

Vertical component synthetic acceleration record sections compliment the horizontal component record sections in Figures 5-23 to 5-28 because the vertical motions show predominantly interface waves. Thus, the vertical component synthetic data provide a natural visual means to distinguish the S-wave arrivals from the interface waves. The largest vertical accelerations observed at any position in the model are normalized to a value of 10; the absolute vertical accelerations are much smaller than the horizontal accelerations given the steep incidence angle of the SV plane wave. Figure 5-29 shows that the arrivals following the refracted SV-waves (which are very weak on the vertical component) are associated with the Stonely wave produced at ~25 m depth and strong Airy phases associated with the fundamental model Rayleigh waves produced at the basin margins. The Airy phase associated with the Rayleigh wave is also the strongest arrival at depths of 10 m (Figure 5-30) and 20 m (Figure 5-31), but the Stonely wave becomes the strongest arrival at a depth of 30 m (Figure 5-32). The Stonely wave train produces the largest vertical accelerations at depths of 40 m (Figure 5-33) and 50 m (Figure 5-34). The largest vertical accelerations occur at 10 m and 20 m depth (Figures 5-30 and 5-31) and are associated with the Rayleigh Airy phase. Vertical accelerations at all depths extending to 50 m are larger than surface vertical accelerations, indicating the dominance of the horizontal propagating interface modes on vertical accelerations.

The 2D synthetic seismograms show that the extended durations observed at the surface are likely associated with a mixture of refracted S-waves, and horizontally propagating surface and interface waves. For shallow depths of 0 m to 20 m the largest accelerations after the near-vertical incidence S-wave directed and reflected arrivals consist of a mixture of refracted S-waves and broadband Rayleigh wave Airy phases. For depths of 30 m and larger, the largest accelerations after the near-vertical incidence S-wave directed and reflected arrivals are associated with refracted S-waves for the portion of the dam located within 1.5 km of the southern glacial scour. At distances > 1.5 km from the glacial scour boundary the Stonely wave produces the largest accelerations for depths of 30 m and larger. The influence of soil nonlinearity on the amplitudes of these interface waves is unknown, although the continued existence of the free surface and
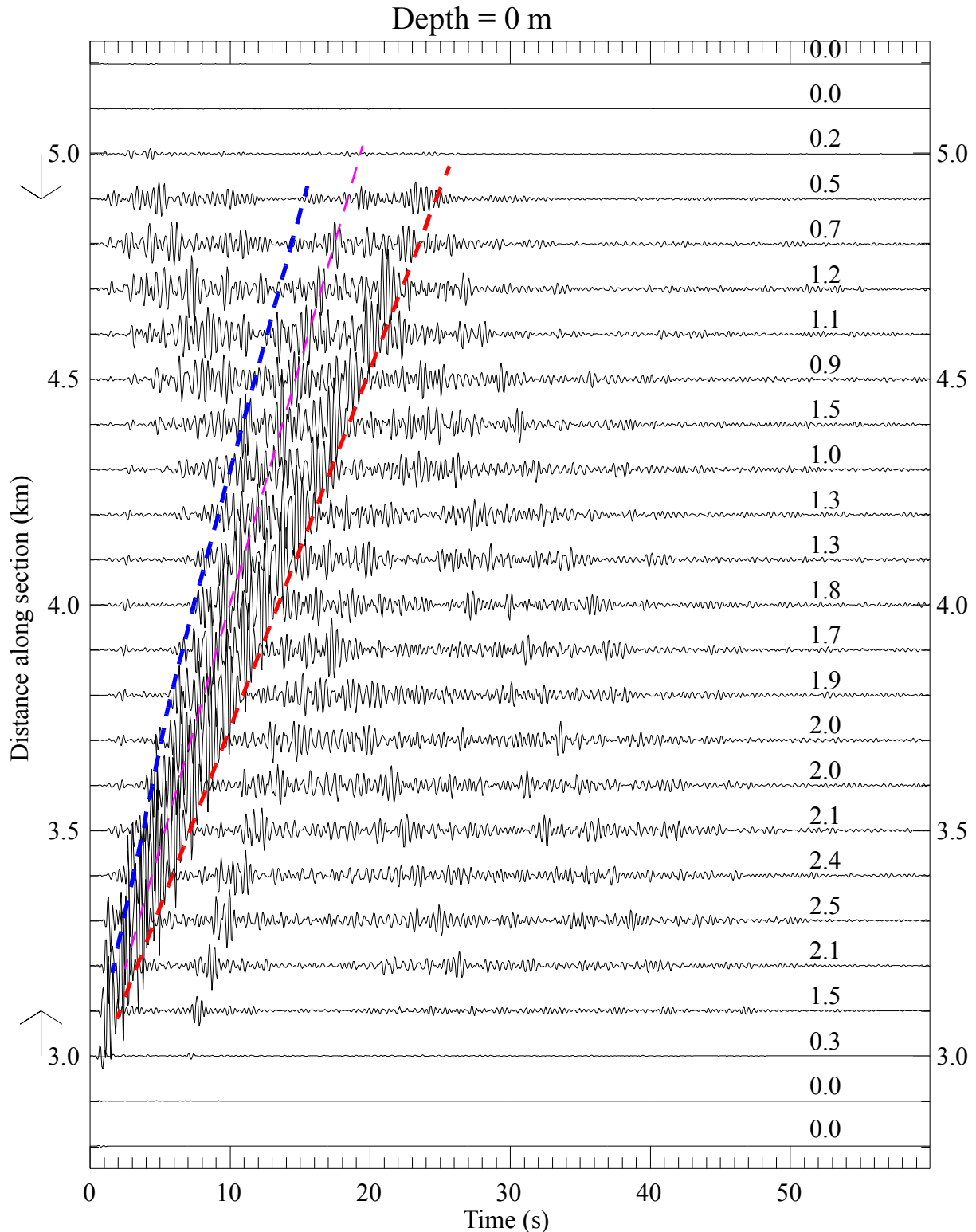
Depth = 0 m

Figure 5-29: Vertical 2D finite-difference acceleration record section z = 0 m.Distances are as shown in Figure 5-22. Peak amplitudes are labels on the right normalized to a maximum value of 10 for all sites in the model. Low-velocity glacial scour sites are between the arrows on the left. Dashed red line shows the end of the basin-edge Airy phase. Dashed blue line is the basin-edge refracted S-wave. Dashed magenta line is the Stonely wave.

Depth =10 m

Figure 5-30: Vertical 2D finite-difference acceleration record section z = 10 m.Distances are as shown in Figure 5-22. Peak amplitudes are labels on the right normalized to a maximum value of 10 for all sites in the model. Low-velocity glacial scour sites are between the arrows on the left. Dashed red line shows the end of the basin-edge Airy phase. Dashed blue line is the basin-edge refracted S-wave. Dashed magenta line is the Stonely wave.
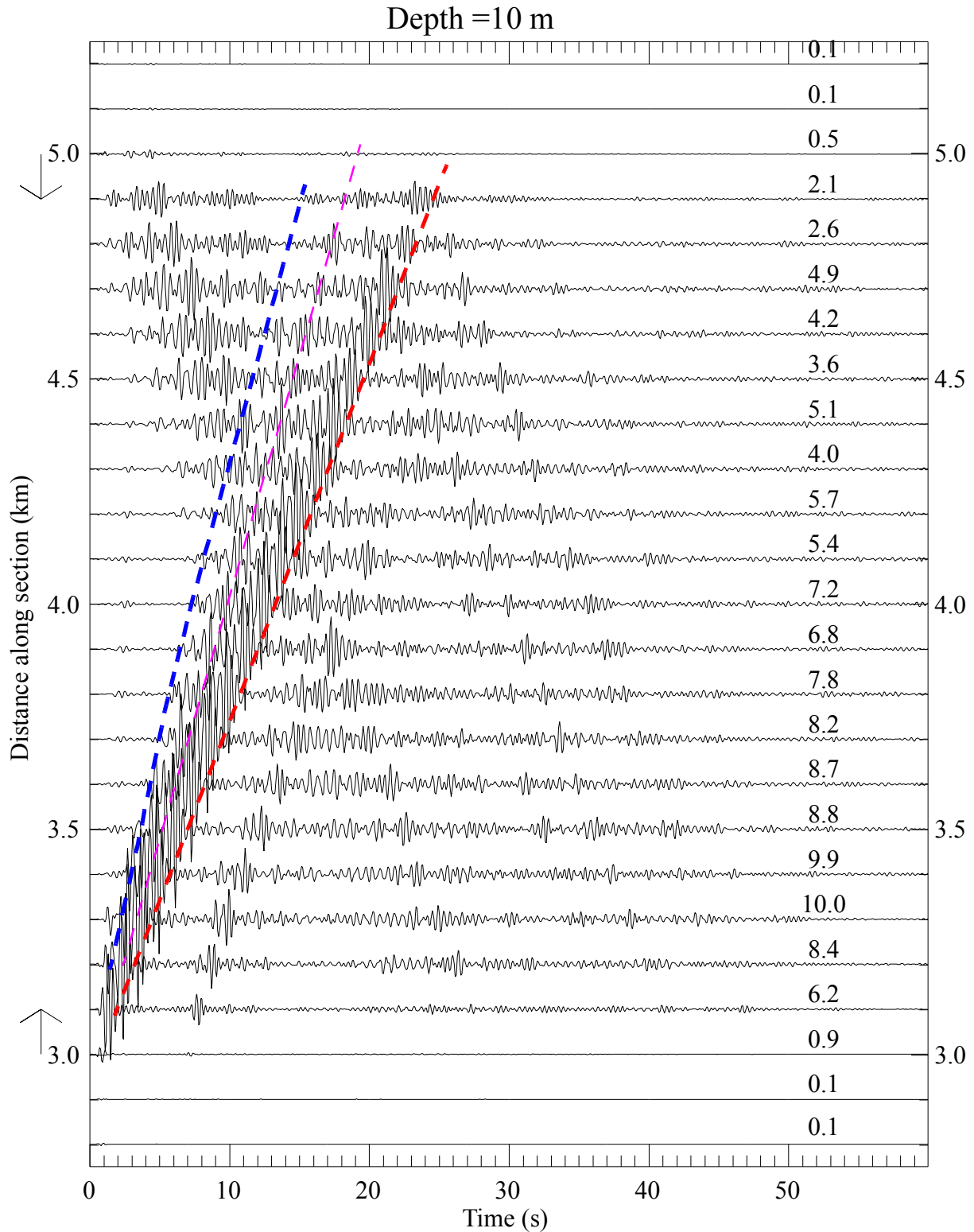
Depth = 20 m

Figure 5-31: Vertical 2D finite-difference acceleration record section z = 20 m. Distances are as shown in Figure 5-22. Peak amplitudes are labels on the right normalized to a maximum value of 10 for all sites in the model. Low-velocity glacial scour sites are between the arrows on the left. Dashed red line shows the end of the basin-edge Airy phase. Dashed blue line is the basin-edge refracted S-wave. Dashed magenta line is the Stonely wave.
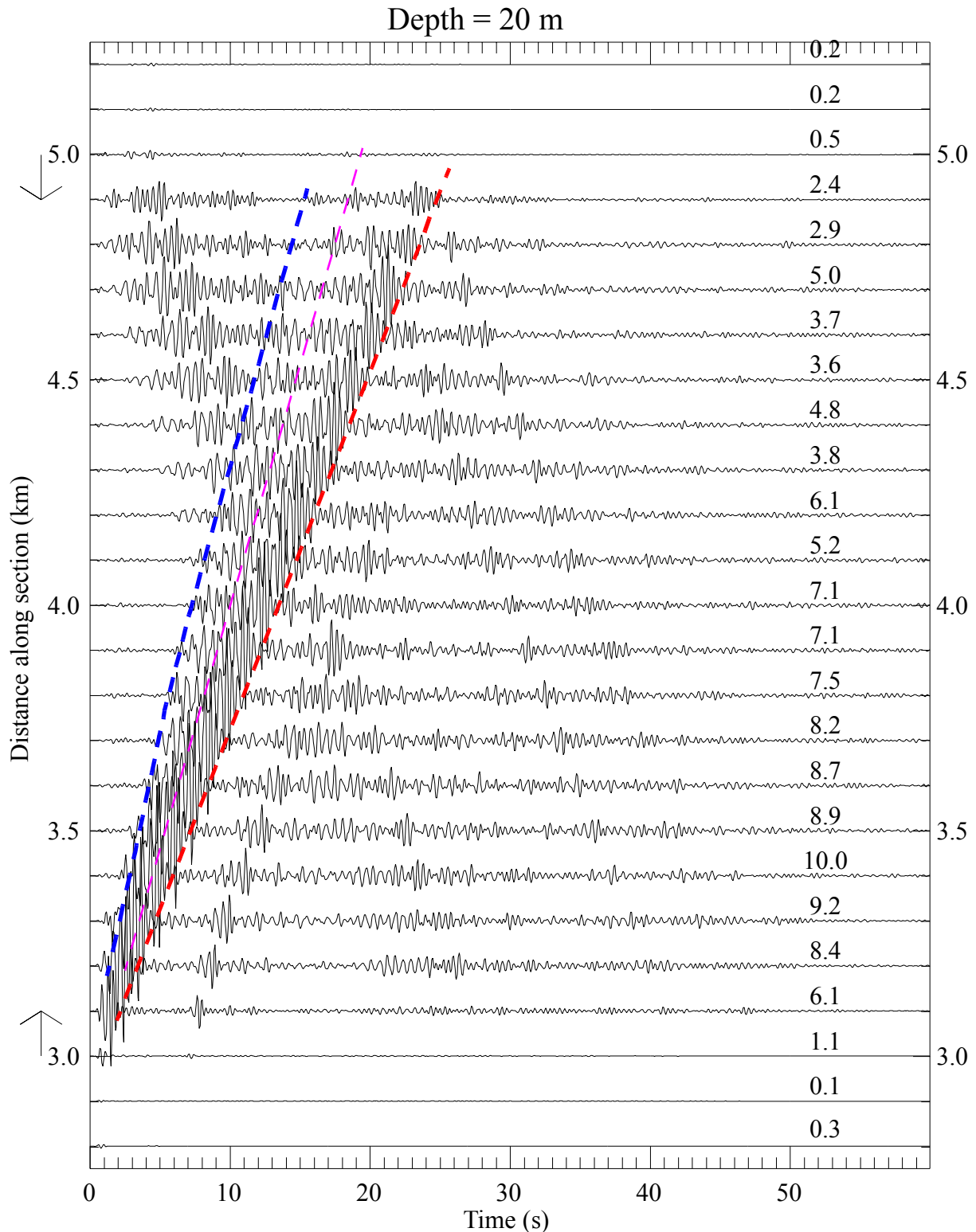
Depth = 30 m

Figure 5-32: Vertical 2D finite-difference acceleration record section z = 30 m. Distances are as shown in Figure 5-22. Peak amplitudes are labels on the right normalized to a maximum value of 10 for all sites in the model. Low-velocity glacial scour sites are between the arrows on the left. Dashed red line shows the end of the basin-edge Airy phase. Dashed blue line is the basin-edge refracted S-wave. Dashed magenta line is the Stonely wave.
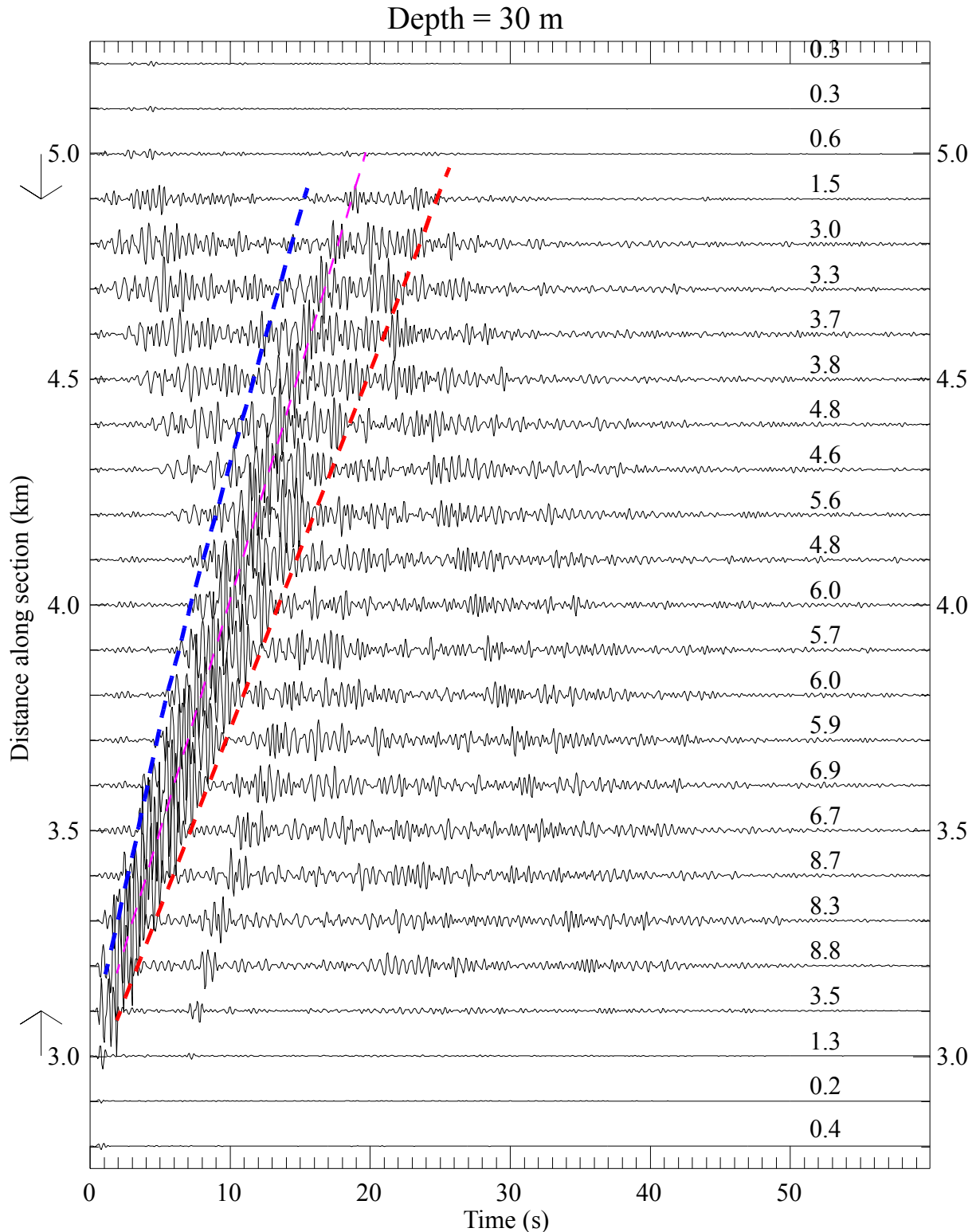
Depth = 40 m

Figure 5-33: Vertical 2D finite-difference acceleration record section z = 40 m. Distances are as shown in Figure 5-22. Peak amplitudes are labels on the right normalized to a maximum value of 10 for all sites in the model. Low-velocity glacial scour sites are between the arrows on the left. Dashed red line shows the end of the basin-edge Airy phase. Dashed blue line is the basin-edge refracted S-wave. Dashed magenta line is the Stonely wave.
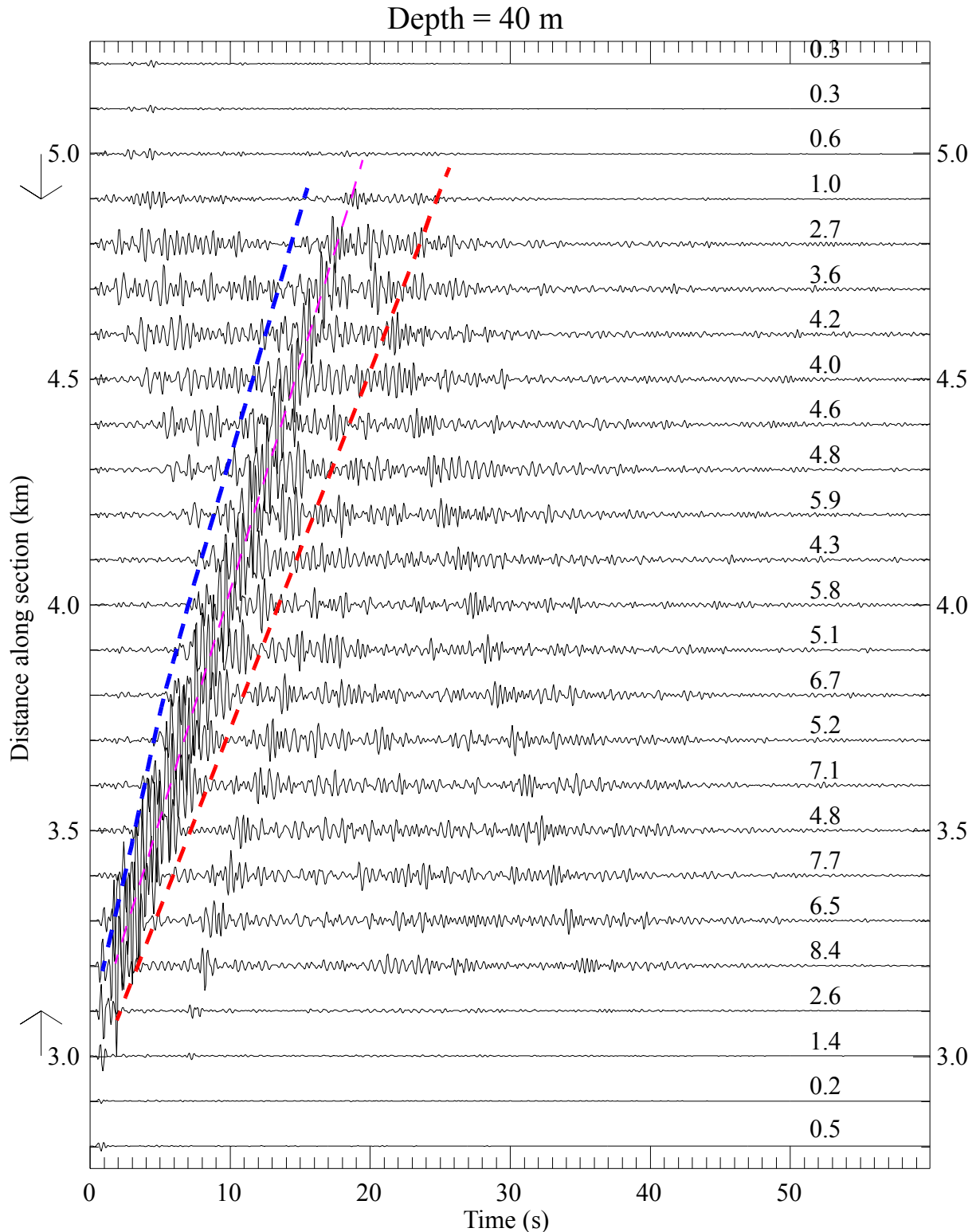
Depth = 50 m

Figure 5-34: Vertical 2D finite-difference acceleration record section z = 50 m. Distances are as shown in Figure 5-22. Peak amplitudes are labels on the right normalized to a maximum value of 10 for all sites in the model. Low-velocity glacial scour sites are between the arrows on the left. Dashed red line shows the end of the basin-edge Airy phase. Dashed blue line is the basin-edge refracted S-wave. Dashed magenta line is the Stonely wave.
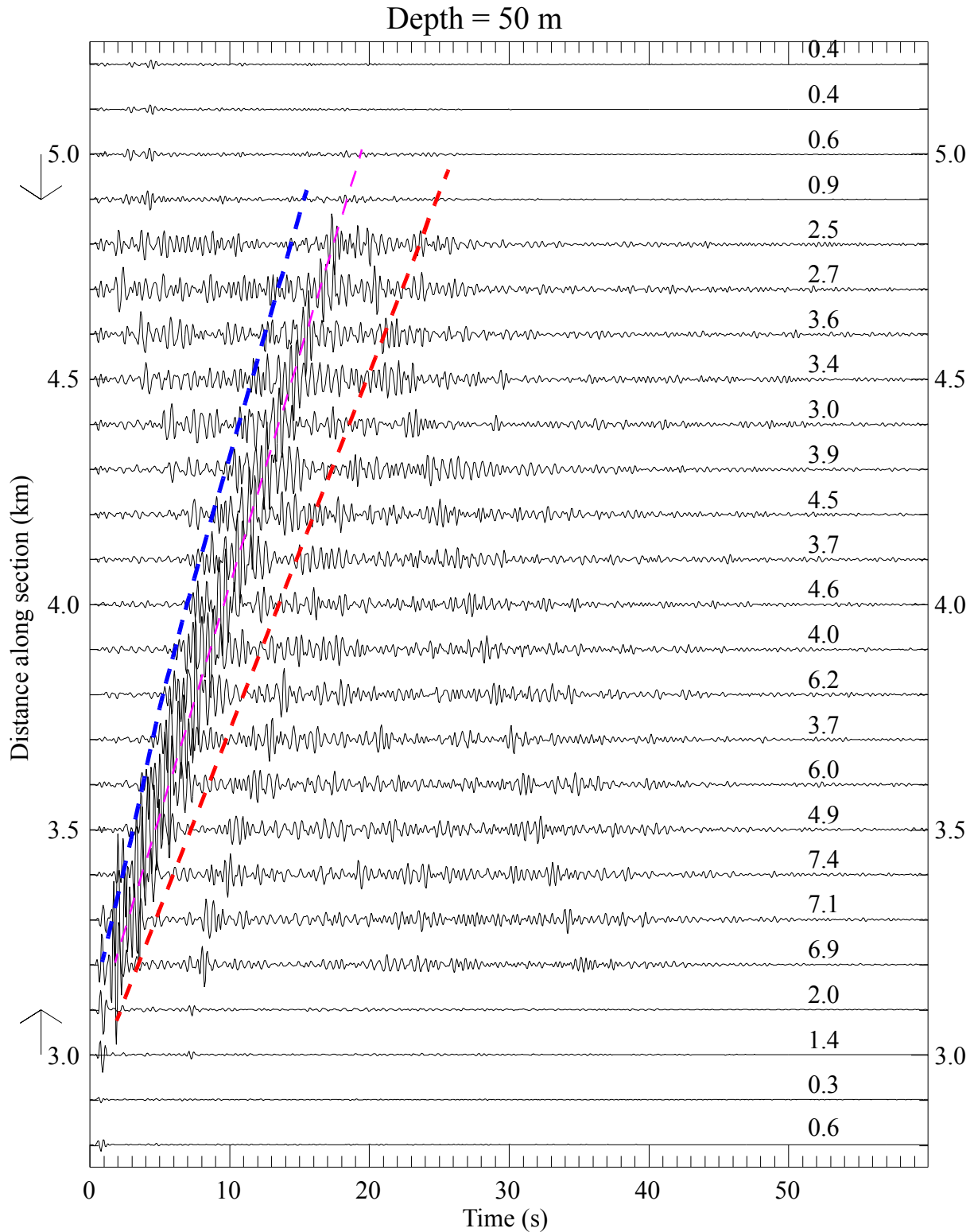
internal velocity discontinuities during modulus degradation suggests that these phases will persist as soils respond nonlinearly. Since a significant amount of energy is propagating horizontally at depths of up to 50 m (Figures 5-23 To 5-28), it is necessary to account for this significant seismic energy in 1D vertical-incident SH nonlinear simulations of nonlinear soil effects, since these codes will not simulate the production of these observed phases. Consequently, it is necessary to include the extended durations in the 1D nonlinear inputs to account for observed, broadband, strong-amplitude extended soil response durations, as discussed in Section 6.

The 2D synthetic seismograms show that there is a critical distance range from the southern margin of the glacial scour where peak horizontal acceleration responses are likely to be amplified relative to most of the embankment section of the dam. This amplification is associated with the constructive interference of the scour basin-edge interface waves, particularly the broadband Airy phases, but also the Stonely wave, with the direct, reflected, and basin-edge refracted S-waves. The critical distance of maximum amplification is a function of the sediment velocities, which limited geophysical measurements (Sirles, 1986) show vary vertically and laterally from near the southern glacial scour margin and the borehole located between stations JLD3 and JLD6. There are no geophysical velocity measurements or ground motion recordings between stations JLD2 (modest amplification) and station JLD3 (strong amplification). Although the 2D velocity model does not contain all the complex features of the glacial scour geometry inferred in Section 2, the 2D finite-difference synthetic results indicate that it is likely that amplifications stronger than those measured at stations JLD3 and JL6 probably occur somewhere between stations JLD2 and JLD3 (along the tallest portion of the embankment section of the dam). Due to the lack of sediment velocity information between stations JLD2 and JLD3, it is not possible to indicate the position or magnitude of the additional amplification relative to station JLD3. It is important to understand that the amplification responses at JLD3 are unlikely to represent the maximum amplification along the embankment portion of the dam between stations JLD2 and JLD3.

The glacial scour S-wave velocity structure at the dam is very similar to the Valley of Mexico in Mexico City (Bodin et al., 1997), except that low-velocities extend ~20 m deeper at Jackson Lake Dam. In the Valley of Mexico, monochromatic, large-amplitude ground motions have durations of

~250 s for M > 6.5 seismic sources located > 200 km from the site (Lomnitz et al., 1999). In contrast, the closest portion of the Teton fault is located ~10 km from Jackson Lake Dam. However, the Valley of Mexico is probably significantly longer and wider than the glacial scour basin at Jackson Lake Dam, although the total extent of the glacial scour basin north of the dam is unknown. Consequently, it is likely that the durations in the central portion of the Valley of Mexico would be somewhat longer than at Jackson Lake Dam because the propagation times from the edges of the very-low-velocity basin to the basin interior would be longer.

While the shallowest ~20 m of sediments at Jackson Lake Dam have S-wave velocities very similar to the Valley of Mexico of 80-100 m/s, the compositions of the shallowest sediments differ. The shallowest sediments in the Valley of Mexico consist almost entirely of lacustrine mud (Lomnitz et al., 1999), but the shallowest sediments at Jackson Lake Dam consist of predominantly fluvial units near the surface grading toward dominantly lacustrine sediments at > 20 m depth (Section 2). Consequently, the shallow sediments at Jackson Lake Dam may respond somewhat differently than the shallow sediments in the Valley of Mexico, particularly at large strains. Bodin et al. (1997) noted that the dominance of clays in the Valley of Mexico surficial deposits probably reduced nonlinear ground motion effects from the 1985 M 8.5 Michocaon earthquake because peak strains were about 0.1%, insufficient to cause significant modulus degradation in clay-dominated soils. Nonlinear soil responses in the surficial fluvial deposits at Jackson Lake Dam are expected to more strongly influence S-wave responses than in the Valley of Mexico because expected strains of > 1% from the nearby M ~7 earthquake (Section 6) are likely to cause modulus degradation. While the impact of nonlinear soil responses on the amplitudes of large-amplitude, broadband Airy phases is unknown, it is likely that nonlinear soil responses will increase the duration of ground motions at the dam, relative to linear soil responses. This is a consequence of dynamic modulus degradation, which reduces shallow S-wave velocities during the earthquake, thereby increasing the travel times of Airy phases propagating in the vicinity of the free surface. For example, for a portion of Jackson Lake Dam located 2 km from a glacial scour lateral terminus, it takes about 20 s for the first basin-edge Airy phase to arrive at the site. If the shallow sediment shear modulus is reduced by a factor of four due to nonlinear response, the S-wave velocity is halved and it will take 40 s for the first basin-edge Airy phase to arrive at the site. Thus, if the shallow sediment section is expected to have a

consistent nonlinear shear modulus reduction, the total duration of ground motions at the dam associated with shallow Airy phases is expected to substantially increase if the shallow sediments respond nonlinearly. With respect to the weak-motion Airy phase responses recorded at the dam, a M 7 earthquake is very likely to produced substantially longer duration Airy phase responses along the embankment portion of the dam (even for linear soil responses) because all edges of the glacial scour will be excited by incident S-waves from all possible azimuths (the dam is located near the middle of the fault) for about 20-30 s (duration of rupture plus delays associated with propagation of basin-edge S-waves from the edge of the low-velocity basin near the fault to the dam). Thus, all the edges of the glacial scour will be strongly excited because substantial S-wave arrivals are almost always certain to be incident at angles to maximize basin-edge Airy phase amplitudes (incident at non vertical angles toward the interior of the scour basin). Rupture of the entire length of the Teton fault will increase Airy phase durations and amplitudes at the dam because about 2/3 of the fault is located south of the dam, and all the S-wave arrivals from the southern 2/3 of the fault are likely to produce strong Airy phase amplitudes along the southern portion of the embankment section (e.g., all these S-waves are incident at non vertical angles pointing into the northern interior of the scour basin). It is important to note that Bodin et al. (1997) emphasize an unusual aspect of very-low velocity basins is the large strains that result from the very short wavelengths and horizontally propagating large-amplitude phases, like Airy phases.

5.5 Summary and Conclusions.

Bedrock ground motions propagating from the Teton fault will be modified by the soil column underlying much of Jackson Lake Dam. Recordings of strong ground shaking at the dam that would be needed to directly estimate this effect do not exist. Instead, ground motions from moderate-magnitude local earthquakes were recorded by three-component broadband velocity seismometers at six locations on the dam, and one location on the right abutment. These recordings were compared to reference sites using the method of spectral ratios.

Ground motions on the north dike at stations 24+00, 30+95, and 52+00 are amplified in the frequency range of 0.2 to 1.5 Hz, in comparison to the right abutment. The duration of ground shaking in this frequency band is substantially prolonged. Ground motions at station 13+00 are

not similarly amplified over this frequency range, nor are the durations appreciably prolonged. Shallow sedimentary basins can generate surface waves and converted body waves which result in this type of site response, as shown in Section 5.4. Low-velocity fluviolacustrine sands, gravels and a northward thickening wedge of fines overly higher-velocity glacial drift and gravels below the north dike (for stations greater than 14+00), which effectively produces a sedimentary basin structure.

High-frequency (>1.0 Hz) ground motions recorded directly above the treated embankment foundation at station 24+00 are observed to be lower in amplitude than outside of the treated zone, consistent with the higher shear-wave velocities obtained from the dynamic compaction and Soil Mix Wall (SMW) treatments. However, for frequencies below 1.0 Hz, substantial amplification and prolonging of duration are observed both inside and outside of the treated zone.

Poorly consolidated, potentially liquefiable fluviolacustrine sands and gravels with shear velocities as low as <300 ft/s (<100 m/s) underlie much of the north dike at stations 13+00 and greater. The site response to strong shaking is expected to be non-linear, in contrast to the observed weak motion response. However, both the weak and strong motion responses are influenced by the same shallow depositional basin structure underlying the dam. While the observed weak motion site response (amplification and prolonging of duration) is consistent with that of a shallow closed basin (2-D and 3-D response), it is not easily explained by a vertically-propagating shear-wave in a horizontally stratified soil column (1-D response). The response of a one-dimensional soil column is difficult to reconcile with the observed response on the dam, which appears to be characterized by surface and interface waves and converted body-waves.

Available computer codes for estimating non-linear site response are based on propagating an incident body wave through a 1-D soil column. These codes will tend to underestimate the observed duration of shaking at Jackson Lake Dam because they do not fully account for the 2-D and 3-D response of the local sedimentary basin (converted phases, surface waves, etc.). In order to better account for the 2-D or 3-D character of the observed weak-motion site response, yet employ available one-dimensional codes for estimating non-linear site response, a hybrid approach is used. This approach incorporates the longer durations observed in the weak motion data to modify the bedrock input motions for use in one-dimensional computer codes.

At stations 12+00 and less, the response to strong ground shaking is not expected to have a substantial non-linear component. The observed weak motion response may therefore be applied to bedrock design ground motions without further modifiation.

This section provided vital information necessary to estimate site-specific rock and soil ground motion responses at Jackson Lake Dam associated with **M** ~7 earthquakes on the Teton fault, the topic of the next section.